A Programmable Platform Enabling Targeted Chromosome Substitution and Cross-Species Stability Profiling

Lei Shi,[1,5] Xiali Yang,[1,5] Mingdi Wu,[1,5] Chengye Zhao,[1,5] Jun Wu,[2,3,4,*] and Erwei Zuo[1,*]

[1]Shenzhen Branch, Guangdong Laboratory for Lingnan Modern Agriculture, State Key Laboratory of Genome and Multi-omics Technologies, Agricultural Genomics Institute at Shenzhen, Chinese Academy of Agricultural Sciences, Shenzhen, Guangdong, China.

[2]Department of Molecular Biology, University of Texas Southwestern Medical Center, Dallas, TX 75235, USA

[3]Hamon Center for Regenerative Science and Medicine, University of Texas Southwestern Medical Center, Dallas, TX 75235, USA

[4]Cecil H. and Ida Green Center for Reproductive Biology Sciences, University of Texas Southwestern Medical Center, Dallas, TX 75235, USA

[5]These authors contributed equally

[*]Correspondence: jun2.wu@utsouthwestern.edu (J.W.), zuoerwei@caas.cn (E.Z.)

Abstract

Chromosome substitution strains (CSS) are critical tools for dissecting complex traits, although iterative breeding steps and intraspecific compatibility requirements limit conventional approaches. Here, we developed an optimized TEAM platform for chromosome replacement combing CRISPR/Cas9–mediated chromosome elimination with microcell-mediated chromosome transfer (MMCT). Using this approach, we substituted the endogenous mouse Y chromosome (chrY) with either the mouse or human Y chromosome. Intraspecies substitutions yielded karyotypically stable embryonic stem cells that supported development into adult males. By contrast, in interspecies CSS, human chrY displayed severe instability and progressive DNA damage. Despite partial transcription of human chrY genes, recipient animals exhibited systemic inflammation, high rates of neonatal death, and poor growth. Reduced CENP-A levels were observed at human chrY centromeres, leading to segregation errors, micronuclei formation, and widespread chromosome rearrangements. This technology enables programmable construction of chromosome substitution models for investigating chromosomal function, genome evolution, and synthetic karyotype design in mammals.

Introduction

Chromosome substitution strains (CSS), in which individual donor chromosomes are introduced into a defined genetic background, have emerged as powerful tools for dissecting complex biological traits.[1] Originally designed for mapping quantitative trait locus (QTL), CSS have since been widely utilized in diverse research areas, including chromosome-specific gene regulation, epistatic interactions, disease modeling, and agricultural trait improvement in both animal and plant systems.[1-8]

Despite their broad utility, conventional CSS construction is constrained by technical and biological limitations, as the process depends on repeated backcrossing and marker-assisted selection over

multiple generations, which is labor-intensive, time-consuming, and prone to unintended recombination.[1,9] Moreover, traditional CSS strategies remain limited to intraspecific systems and cannot accommodate chromosomes from different species or synthetic origins for which reproductive or centromeric compatibility cannot be assumed.[10-12] With rapid advances in synthetic genomics, humanized disease models, and interspecies reproductive engineering, the need for flexible, scalable, and breeding-independent strategies becomes increasingly urgent to keep pace with potential applications for CSS systems.

At present, new methods in genome editing and chromosome engineering have opened new avenues for developing more efficient and flexible chromosome substitution strategies. In particular, CRISPR/Cas9-mediated chromosome elimination has emerged as an effective tool for selectively removing entire chromosomes by targeting lineage-specific repetitive elements or centromeric sequences.[13] This strategy has been widely applied in a variety of research fields, such as elimination of extra chromosome 21 in cells from individuals with Down syndrome[14], assessment of chromosome loss in CRISPR/Cas9 engineered T cells[15], and establishment of mosaic loss of Y chromosome (mLOY) disease models[16]. Alternatively, microcell-mediated chromosome transfer (MMCT) offers a robust approach for delivering intact, natural or engineered donor chromosomes into recipient cells via microcell fusion, and has been used to introduce native or artificial chromosomes in mammalian systems.[6,17] Together, these technologies lay the foundation for overcoming temporal and biological constraints associated with conventional CSS production, enabling rapid, precise chromosome substitutions, even between different species.

Combining CRISPR/Cas9-mediated chromosome elimination with MMCT, we developed an optimized chromosome substitution platform that allows replacement of mouse Y chromosome (chrY) with a donor chrY of either mouse or human origin. We then applied this platform for in vitro and in vivo comparisons of intraspecies and interspecies chrY substitution strains to examine cross-species chromosome stability and the phenotypic consequences of chrY substitution in mice. We also investigated the potential mechanism underlying interspecies chrY instability. Beyond demonstrating the scalability and robustness of the platform for CSS construction across species, our study also highlights its utility as a functional assay for chromosomal incompatibility and centromere evolution, thus broadening the potential for CSS application in mammalian systems.

Result

Intraspecies Y Chromosome Substitution via TEAM

To overcome limitations of conventional CSS generation approaches, we developed the TEAM (Targeted chromosome Elimination And Microcell-mediated chromosome transfer) platform (Figure 1A). As previous studies have shown that mouse artificial chromosomes (MACs) constructed from native chromosomes exhibit high stability in adult tissues and hematopoietic cells in mice,[18,19] we first examined the stability of CSS mice generated by TEAM using the mouse chrY as a proof-of-concept. We tagged the donor chrY by co-transfecting male DBA/2 ESCs with plasmids encoding Cas9, a donor construct containing a CAG-puromycin-GFP (CAG-puro-GFP) cassette flanked by homology arms, and an sgRNA targeting the region between *Uty* and *Ddx3y* (Figures S1A-S1C). After selecting cells with puromycin, genomic PCR showed that 7 of the 18

clones (38.9%) were successfully targeted (Figure S1D). Droplet digital PCR (ddPCR) confirmed single-copy integration of the selection marker at the expected locus in clones #9, #11, #15, and #17, without off-target recombination events (Figure S1E). These clones, named DBA-puro-GFP, also showed strong GFP expression (Figure S1F).

To obtain low-passage chrY recipient cell lines, Cas9 mRNA and two sgRNAs targeting *Spermiogenesis-specific transcript on Y 2* (*Ssty2*), which spans over 30 repeat sequences on the long arm of chrY, were injected into C57BL/6 zygotes (Figure S2A). The treated embryos were then cultured in vitro to generate mouse ESCs (mESCs). Among the 11 resulting mESC clones, three lacked mouse chrY (Figures S2B and S2C). These chrY-deficient clones, designated as C57 XO, exhibited a 39-chromosome karyotype with a single X chromosome (Figures S2D and S2E), while the wild-type C57BL/6 mESCs harbor 40 chromosomes. Next, we fused DBA-puro-GFP #11 ESCs with CHO cells stably expressing tdTomato (CHO^{td}) (Figure 1B) to create hybrids ($CHO^{td}DBA^{GFP}$). Next, we utilized the conventional MMCT protocol to generate microcells. The $CHO^{td}DBA^{GFP}$ cells were treated with colchicine to induce micronucleation. Then, cells were treated with Latrunculin B to disrupt cytoskeletal integrity. Microcells were isolated by Percoll gradient centrifugation. The $CHO^{td}DBA^{GFP}$-derived microcells were then fused with C57 XO mESCs. Following puromycin selection, GFP-positive mESC clones (designated as C57 XY^{D}) were obtained at a frequency of 1×10^{-6} (Figure 1C). Fluorescence in situ hybridization (FISH)/Whole genome sequencing (WGS) analysis indicated that a significant portion of chrY sequence could be detected in C57 XY^{D} mESCs (Figures 1D and 1E). Notably, all C57 XY^{D} mESC lines exhibited a normal 40-chromosome karyotype (Figures 1E and 1F). However, consistent with previous studies,[20] WGS analysis revealed substantial deletions on the transferred chrY. Specifically, C57 XY^{D} #1 showed ~40.3% of chrY, while C57 XY^{D} #2 had a ~38.3% deletion (Figure 1G), and other C57 XY^{D} lines showed similar levels of chrY sequence loss.

Bulk RNA-seq analysis showed that C57 XY^{D} mESCs had transcriptomic profiles nearly identical to those of male C57BL/6 mESCs, with a strong correlation (Pearson r = 0.99 for C57 XY vs. C57 XY^{D} #1) (Figure 1H). Combined with immunostaining for pluripotency markers OCT4, SOX2, and SSEA1, these results suggest that intraspecific chrY transfer had minimal effect on gene expression in mESCs (Figures S3). The overall results support that the combined use of CRISPR/Cas9-mediated chromosome elimination and MMCT is a viable approach for intraspecies chrY substitution.

MMCT Induced Micronuclei Formation Drives DNA damage

Micronuclei[21], small, separate nuclear structures formed when chromosomes lag during cell division, are both a sign and a cause of genomic instability. These structures are more fragile than normal nuclei, and their DNA often replicates out of sync with the rest of the cell, leading to DNA damage and chromosomal fragmentation.[22,23] In MMCT, colchicine is used to promote micronucleation formation. To assess how this step affects chromosome integrity within the MMCT workflow, we first examined the nuclear envelope stability of colchicine-induced micronuclei. We created a CHO^{CN} cell line that stably express mCherry-tagged nuclear localization signals (mCherry–NLS). These CHO^{CN} cells were fused with DBA-puro-GFP #11 mESCs to form $CHO^{CN}DBA^{GFP}$ hybrid cells. In colchicine-treated $CHO^{CN}DBA^{GFP}$ cells, we observed loss of mCherry–NLS signal in

micronuclei, indicating nuclear envelope instability. In contrast, HBSS-treated control cells maintained the mCherry signal in cell nuclei (Figure S4A). Additionally, immunostaining for γH2AX, a marker of DNA damage, revealed damage in 26.7% of micronuclei in colchicine-treated cells (Figures S4B and S4C). WGS analysis further confirmed the extent of the damage: colchicine-treated CHO^{td}DBA^{GFP} cells had 8,596 single nucleotide variants (SNVs) and 7,982 insertions/deletions (indels) not present in the control group (Figure S4D). To further evaluate whether colchicine-induced DNA damage is dose- or time-dependent, we quantified γH2AX signals in CHO^{td}DBA^{GFP} cells treated with varying colchicine concentrations (0, 50, 75, and 200 ng/ml) and exposure times (12–72 h). Prolonged exposure significantly increased DNA damage, with multiple conditions showing higher γH2AX signals at 72 h compared with 12 h. In CHO^{td}DBA^{GFP} cells, higher colchicine doses also induced significantly greater DNA damage (Figure S4E and S4F).

These findings demonstrate that MMCT, through colchicine-induced micronuclei formation, disrupts the nuclear envelope and causes widespread DNA damage in a dose- and time-dependent manner. This mechanism likely contributed to the chrY fragmentation seen in C57 XY^{D} mESCs.

Generation of intraspecies Y-Chromosome-replaced mice via tetraploid complementation

To test whether XY^{D} mESCs could be used to generate live animals, we injected C57 XY^{D} #1 mESCs into tetraploid B6D2F1 blastocysts. This approach successfully produced 28 viable, GFP-positive pups (Figure 2A; Table S1), confirming the developmental competence of the modified mESCs. To evaluate the effects of chrY transfer, we compared the growth and development of C57 XY^{D} mice to wild-type C57BL/6 and C57 XO mice (generated using C57 XO mESCs). All groups showed normal growth into adulthood (Figures 2B and 2C). WGS confirmed that the C57 XY^{D} mice carried the mouse chrY (Figure 2D), and all developed as males (Figure 2E). Histological analysis of E12.5 embryos revealed the presence of gonocytes in the genital ridges (Figure 2F), indicating active and functional *Sry* gene expression.[24]

Further sequencing showed that the chrY DNA sequences in C57 XY^{D} mice closely matched those of the original mESCs (Figure 2G), suggesting that the chromosome remained stable throughout development. The DNA deletions seen in the mESCs were therefore likely caused by the MMCT process itself, rather than developmental instability. These findings further reveal that although MMCT introduces micronucleus-associated DNA damage, such damage does not compromise the long-term stability of transferred chromosomes. Overall, these results demonstrate the feasibility of using the TEAM strategy for stable, intraspecific Y chromosome replacement in mice, and support its broader use for studying chromosome stability after chromosome transfer.

TEAM enables replacement of mouse Y chromosome with human Y chromosome in mESCs

We next applied TEAM platform to test cross-species chromosome replacement by substituting mouse chrY with human chrY. We first inserted a CAG-puro-GFP tag between two genes (DDX3Y and UTY) on the chrY in H1 human ESCs, creating three labeled clones (H1-puro-GFP; Figure S5). Using one of these clones, we fused H1-puro-GFP #1 with tdTomato-expressing A9^{td} cells to create a donor cell line (A9^{td}H1^{GFP}) capable of providing microcells for chromosome transfer (Figure 3A).

As with mouse chromosome transfers, colchicine-treated A9^{td}H1^{GFP} cells showed signs of DNA damage, confirmed by γH2AX staining and WGS (Figure S4). We then fused these donor microcells with C57 XO mESCs. After puromycin selection, 29 GFP$^+$ mouse stem cell lines were recovered (Figure 3B), at a frequency of 1–3 × 10^{-6}. Karyotyping showed that 14 of these lines had a normal mouse chromosome number (40), while the rest had around 80 chromosomes, likely due to cell fusion events (Figure 3C).

FISH analysis confirmed that the human chrY was successfully transferred and maintained as a separate chromosome in all 14 normal karyotype lines, now referred to as C57 XY^H mESCs (Figure 3D). However, WGS revealed substantial deletions on the transferred human chrY: C57 XY^H #3 had lost ~87.3% and C57 XY^H #5 had lost ~72.6% of human chrY (Figures 3E and 3F). Importantly, there were no copy number changes in mouse autosomes or the X chromosome, showing that only the transferred human chrY was affected. Despite these deletions, RNA-seq showed strong gene expression similarity between C57 XY^H mESCs and wild-type male C57 XY mESCs (Pearson r = 0.97 for XY^H #3 and 0.98 for XY^H #5; Figure 3G). Immunostaining confirmed continued expression of key pluripotency markers (OCT4, SOX2, and SSEA1; Figure S6). However, the human chrY showed poor stability over time. Flow cytometry revealed that in some C57 XY^H lines, GFP expression rapidly decreased with cell passages. By passage 7, nearly all C57 XY^H #4 cells had lost GFP. In contrast, C57 XY^H #3 and #5 retained 40% and 10% GFP$^+$ cells after 10 passages, while mouse-derived C57 XY^D cells remained stable (Figures 3H and 3I).

In summary, although replacing the mouse chrY with a human chrY had little effect on mESC self-renewal and gene expression, the human chrY was much less stable in mESCs after transfer.

Neonatal death and poor growth in mice carrying the human Y chromosome

To test if mESCs with a human chrY (XY^H mESCs) could produce live animals, we injected C57 XY^H mESCs into tetraploid B6D2F1 blastocysts. This resulted in 122 pups (Figure 4A; Table S1), showing that the human chrY did not prevent full-term embryonic development. However, unlike mice carrying the mouse chrY (C57 XY^D), the C57 XY^H pups showed mixed GFP expression—some were GFP-positive, some GFP-negative, and others had patchy (mosaic) expression (Figures 4A and 4B). Of the 112 pups from C57 XY^H #3, 87.5% were GFP$^+$, 7.1% were GFP$^-$, and 5.4% showed mosaic expression. In contrast, pups from C57 XY^H #5 were mostly GFP$^-$ (60%). To rule out chimerism (the presence of mixed genetic background), we performed SNP genotyping and confirmed all pups carried only the C57BL/6 genome (Figure S7), meaning the variation in GFP was due to instability or loss of the human chrY.

GFP$^+$ C57 XY^H mice showed high neonatal death and poor growth after birth. At birth, body weights were similar across all groups (Figure 4C). However, 39.3% of GFP$^+$ pups had breathing issues or birth defects like omphalocele, and died soon after birth (Figure 4D). Surviving pups raised by foster mothers showed poor suckling in both GFP$^+$ and some GFP$^-$ groups, leading to death from dehydration within 48 hours. Only 21.2% of GFP$^+$ and 63.6% of GFP$^-$ pups had visible milk intake, compared to 100% of wild-type mice (Figure 4D; Table S1).

Pups that survived still showed growth problems. From postnatal day 7 to 15, GFP$^+$ mice grew significantly slower than wild-type males, while GFP$^-$ pups had slightly lower, but not significantly

different, growth rates (Figure 4E). Survival analysis showed GFP^- mice lived longer than GFP^+ mice (Figure 4F). Only one GFP^+ mouse survived to day 37, weighing just 4.9g—much smaller than its GFP^- littermates, which averaged 17.67g (Figure 4G).

These results show that replacing the mouse chrY with a human chrY causes serious health problems postnatally, including high death rates after birth and impaired growth.

Transcriptomic alteration and inflammation in mice with a human Y chromosome

Because the C57 XY^H GFP^+ mice showed serious health issues, we examined how the human chrY affected their gene expression and immune response. We performed WGS and bulk RNA-seq on eight organs, including cortex, cerebellum, olfactory bulb, heart, liver, spleen, lung, and kidney, from six XY^H mice at different ages (P1 [n = 1], P9 [n = 2], P11 [n = 1], P12 [n = 1], and P15 [n = 1]). Variant calling in WGS data revealed deletions in three chrY genes, *DDX3Y*, *USP9Y*, and *UTY*, in all tissue samples of the P12 mouse, and *UTY* was deleted in all tissues of the P15 mouse. Other timepoints showed no major deletions in the seven key Y-linked genes we analyzed (*VCY1B, VCY, UTY, USP9Y, TMSB4Y, NLGN4Y*, and *DDX3Y*). Since the deletions appeared across all tissues, they likely occurred early in development prior to organogenesis. The differences among XY^H mice suggest that these deletions were derived from random events. Subsequent RNA-seq analysis using the same samples confirmed that these human chrY genes were still expressed in all XY^H mice, though at varying levels. Expression of deleted genes like *DDX3Y* and *USP9Y* was lower, as expected. Interestingly, *VCY1B* was the most strongly expressed gene across tissues. When compared to human data[25], expression levels in mice were similar, suggesting the mouse cell environment supports normal expression of human chrY genes (Figure 5A).

Next, we studied the overall changes in gene expression. Comparing XY^H and wild-type mice across tissues revealed 4,278 differentially expressed genes (DEGs), with the liver showing the most (1,335) and the cortex the fewest (121). Many of the upregulated genes were related to inflammation, immune cell movement, and cytokine production. Genes linked to the senescence-associated secretory phenotype (SASP)—such as *Il1a, Il1b, Il6, Ccl2,* and *Cxcl2*—were also significantly increased (Figures 5B, 5C, S8B and S8C). In the liver, downregulated genes were mostly involved in cell division and cytoskeleton organization, suggesting impaired cell growth (Figure 5B). Consistent with the transcriptomic data, immune cells, $CD45^+$ lymphocytes and $CD68^+$ macrophages, were more abundant in the liver, heart, kidney, and lungs of XY^H mice than in wild-type controls. Only the cortex showed a mild but noticeable increase in macrophages (Figures 5D, 5E and S8D).

In summary, our results demonstrate that the transferred human chrY experienced random gene deletions and triggered widespread changes in mouse transcriptome. These included strong inflammatory responses and immune cell infiltration across multiple organs, likely contributing to the health problems observed in C57 XY^H GFP^+ mice.

Instability of human Y chromosome in Mice

Next, we examined how the human chrY behaves across different stages and tissues during mouse

development. In C57 XY^{H} GFP^{+} pups, GFP (used to trace the human chrY) was detected in most major organs, including the brain, heart, liver, lungs, kidneys, and pancreas. The spleen, however, showed little to no signal (Figure 6A). When analyzing tissue sections, we found significant variation in the proportion of GFP^{+} cells between organs, with the forebrain showing the highest levels (Figures 5E, 6B, 6C, S8D). Real-time PCR targeting the human *UTY* gene confirmed this uneven distribution and showed that expression levels also varied within individual organs (Figure 6D).

WGS analysis of both GFP^{+} and GFP^{-} XY^{H} mice revealed that in GFP^{-} animals, the human chrY was either completely lost or present only in fragments (Figure 6E). In contrast, GFP^{+} mice retained the human chrY, but it showed different degrees of DNA damage depending on the tissue and the individual (Figures 6E and 6F). These results are consistent with earlier observations of inconsistent gene expression from the transferred chrY (Figure 5A). Further comparisons at different developmental timepoints revealed that damage to the human Y chromosome increased with age and was not uniform across tissues (Figure 6F and 6G).

Altogether, these results show that the human chrY, unlike mouse chrY, when introduced into mice via MMCT, undergoes persistent DNA damage and progressive instability in vivo.

Structural instability and complex rearrangements in transferred human Y chromosome

To further investigate the instability of the transferred human chrY, we analyzed structural changes and copy number alterations using WGS data from C57 XY^{H} #3 mESCs (passage 9), tail samples from two C57 XY^{H} #3 mice (P8 and P13), and spleen tissues from three mice at different ages (E18.5, P0, and P7) (Figures 3F, 6E, 6F). Compared to mESCs, tail samples showed additional rearrangements in human chrY, and spleens exhibited even more complex and extensive copy number alterations (Figure 7A). In contrast, no such changes were seen in mouse chrY from control C57 XY^{D} #1 mice (Figure 7B), highlighting the specificity of these alterations to the human chromosome.

These patterns of instability, including copy number variations, are often linked to DNA damage from errors in chromosome segregation and micronuclei formation.[23] Supporting this, FISH analysis combined with γH2AX staining showed that 44.3% of micronuclei in C57 XYH mESCs contained human chrY, and 58.3% of those were γH2AX-positive, indicating DNA damage (Figures 7C, 7D). This aligns with RNA-seq findings of downregulated genes related to the mitotic cycle, microtubule structure, and checkpoint signaling in the liver (Figure 5B; Table S4). Centromere function is crucial for correct chromosome segregation. Although human chrY includes repetitive alphoid DNA, it lacks functional CENP-B boxes.[26-28] To assess centromere activity, we measured CENP-A (a key centromere protein) intensity at the human chrY in C57 XY^{H} mESCs and compared it with mouse chrY in C57BL/6 cells. After normalizing for total CENP-A levels per cell, we found that ~2.7% (6/219) of human chrY lacked detectable CENP-A signal (Figure 7E and 7F). Further FISH analysis revealed that ~83.3% (5/6) of these chromosomes were involved in inter-chromosomal rearrangements, containing segments from both human chrY and mouse chromosomes (Figure 7E). Overall, the human chrY showed significantly weaker CENP-A signal compared to native mouse chrY (Figures 7E, 7G), consistent with earlier reports that low CENP-A leads to mis-segregation.

[26,27]

These findings indicate that transferring human chrY into mice results in ongoing chromosomal instability, marked by structural rearrangements, persistent DNA damage, and variation between tissues. Defective centromere formation, due to reduced or absent CENP-A and inter-chromosomal fusions likely cause segregation errors and micronuclei formation, further driving the instability of human chrY in a mouse background. These insights reinforce the importance of centromere compatibility in construction of karyotype-stable interspecies CSS and highlight TEAM platform's utility for assessing chromosomal barriers across species.

Discussion

This study establishes TEAM, a scalable and modular chromosome substitution platform that integrates CRISPR/Cas9-mediated chromosome elimination with MMCT to provide a versatile toolkit for precise chromosome replacement in both intra- and interspecies contexts. By eliminating the need for backcrossing, reducing recombination-induced structural variations, and expanding the scope of CSS beyond species boundaries, this approach overcomes key limitations of traditional CSS systems, thus representing a major paradigm shift in chromosome-scale engineering.

Using this system, we successfully substituted endogenous chrY in C57BL/6 mESCs with an exogenous chrY from either DBA/2 or H1 ESCs. In intraspecies CSS, all mice generated via tetraploid complementation (C57 XY^D) displayed uniform GFP expression, and WGS analysis confirmed that these animals harbored a chrY nearly identical to that in the original mESCs. Although partial DNA damage was detected on the transferred Y chromosome, transcriptomic analysis revealed no significant differences between C57 XY^D and male C57BL/6 mESCs. Two factors may contribute to this observation. First, the mouse chrY encodes a limited number of protein-coding genes, and the successful generation of tetraploid complementation mice from Y-null mESCs (Figure 2C) indicates that these genes play only a minor role in maintaining pluripotency. Second, the transcriptomic similarity suggests that the TEAM-mediated chromosome substitution process does not cause extensive perturbations to the global gene expression landscape or to other chromosomes within the chrY recipient cells. The successful replacement of mouse chrY and generation of viable offspring underscore the TEAM system's developmental compatibility. In contrast, our tests involving interspecies chrY replacement resulted in pronounced genomic instability, developmental failure, and postnatal lethality, despite detectable expression of human Y-linked genes. These different outcomes between intra- and interspecies CSS highlight the power of TEAM to enable efficient chromosome substitution, while also allowing dissection of the boundaries of chromosomal compatibility among species.

Mechanistically, the instability of human chrY in the murine background is driven, in part, by reduced levels of the histone H3 variant, CENP-A, at the human centromere, a key determinant of centromere identity.[29] This phenomenon aligns well with prior evidence showing that insufficient CENP-A disrupts kinetochore formation and leads to chromosome mis-segregation.[26,27] Both centromere DNA sequence and protein components including CENP-A are rapidly evolving.[30,31] In humans, centromeres are composed mainly of 171-base pair α-satellite higher-order repeats, whereas centromeres in mice consist of more uniform 120-bp minor satellite repeats, surrounded by

less-ordered 234-bp major satellite arrays.[11,29,32] Apart from differences in DNA sequence, human CENP-A shares less than 60% sequence identity with canonical H3 and shows significant divergence across species, especially within its highly variable N-terminal domain.[33] Molecular conflicts disrupting centromere maintenance has been reported to induce Xenopus hybrid inviability.[34] These data suggest that evolutionary divergence between species may impair murine CENP-A binding on human chrY in mouse cells, contributing to its instability after transfer.

We observed severe biological consequences of chrY instability at both the cellular and organismal levels. In ESCs and mouse tissues, human chrY was progressively lost or rearranged, while animals carrying the substituted chrY exhibited systemic inflammation, postnatal growth retardation, and perinatal lethality. Since DNA damage and genomic instability are known to activate immune and senescence pathways, e.g. cGAS-STING, NF-κB, and ATM signaling[35-37], we propose that the instability of the transferred chrY triggers chronic inflammation, which subsequently drives the observed developmental defects. Interestingly, although we found that several genes on human chrY were highly expressed in the mouse cortex, no significant increase in inflammatory markers was detected in this brain region of C57 XY^{H} GFP^{+} males compared to wild-type males. Notably, activated T cells are known to cross the blood–brain barrier under a variety of inflammatory or antigen-driven conditions, including autoimmune and neurodegenerative states.[38,39] Thus, the absence of immune infiltration in the cortex, despite robust chrY gene expression and the highest retention of the transferred chrY among all examined tissues, indicates that chrY-derived proteins alone are insufficient to elicit an adaptive immune response. Rather, it is likely the genomic instability and resulting cellular stress from the damaged human chrY that drive the pathological response. These findings highlight the importance of maintaining chromosomal integrity in interspecies CSS and further reinforce the link between chromosome instability and inflammatory disease phenotypes. In addition, many phenotypes of C57 XY^{H} mouse are also characteristic of mice with imprinting abnormalities.[40] This raises the possibility that defects in genomic imprinting within the C57 XY^{H} mESCs may contribute, at least in part, to the observed developmental and postnatal abnormalities. Future studies should systematically evaluate DNA methylation and allelic expression at key imprinting regions in C57 XY^{H} mESCs to clarify the relationship between human chrY substitution and potential genomic imprinting disorders.

Interestingly, earlier studies involving mice carrying native human chromosomes or human artificial chromosomes (HACs) did not report the same level of developmental defects or postnatal mortality that we observed in the current study.[19,41] This difference likely reflects fundamental variations in the stability of transferred chromosomal material. Previous work has mainly focused on autosomes or autosome-derived HACs,[42] which contain both CENP-A and CENP-B centromeric binding sites.[27,42] CENP-B binds to specific 17-base-pair repetitive DNA motifs known as CENP-B boxes. This interaction enhances the fidelity and stability of human centromere function.[27] In contrast, human chrY lacks CENP-B boxes, making it inherently more prone to segregation errors and DNA damage.[27] As a result, despite some degree of instability reported in transferred human autosomes or HACs in mouse models, the genomic stress they cause is typically not severe enough to trigger widespread inflammation or developmental failure such as we observed with human chrY transfer. Our findings emphasize that the structural features of transferred chromosome, especially at the centromere, are critical determinants of its long-term stability and biological impact.

Notably, although chrY was used for proof-of-concept demonstration of TEAM capabilities in

chromosomal transfer, in principle, this platform could be applied to autosomes, artificial chromosomes, or synthetic constructs bearing engineered epigenetic or centromeric features. The ability to selectively remove and replace entire chromosomes in a defined and controlled manner provides a powerful tool for autosomal replacement, construction of humanized disease models, exploration of species-specific epigenetic barriers, and construction of synthetic karyotypes.

Several limitations of our current study warrant consideration. First, MMCT involves colchicine treatment and micronuclei formation, which can cause genome-wide DNA damage, as we observed via γH2AX staining and structural variant analysis. Therefore, protocol optimization or exploring micronucleation independent chromosome transfer approaches may partially mitigate procedure-induced DNA damage. Isolated metaphase chromosome transfer (iMCT) and flow-sorted chromosome transfer (FSCT), have been reported to function without relying on micronucleation.[43-45] Furthermore, an improved version of MMCT (R-MMCT) has been reported.[46] In this method, colchicine exposure time was shortened from 48-72 hours to 7-9 hours. This modification prevents micronucleus formation during chromosome preparation and markedly reduces DNA damage. These findings provide an important conceptual framework for future refinement of our TEAM platform. Improving the integrity of the nuclear envelope and optimizing centromere compatibility, potentially achieved via artificial centromere engineering or chimeric CENP-A rescue, may enhance the fidelity of interspecies chromosome transfer. Additionally, future studies will further explore the adaptability of TEAM platform to other autosomes or X chromosome.

In conclusion, the TEAM platform establishes a framework for constructing CSS models. While we acknowledge that the current procedure may introduce DNA damage to the recipient chromosome, the system provides a critical proof-of-concept for targeted replacement of chromosomes, or at least chromosomal fragments, in mammalian cells. Notably, our work represents the first successful interspecies chromosome substitution, demonstrating the feasibility of cross-boundary chromosomal engineering. Despite the technical challenges, TEAM offers a versatile and scalable toolkit that opens new avenues for investigation of chromosome biology across species.

Method

Animals

C57BL/6 female mice aged 4 weeks and ICR (CD1) female mice aged 8 weeks were purchased from Guangdong Medical Laboratory Animal Center. 8-week-old B6D2F1 female mice and 8-week-old DBA/2 male mice were purchased from Vital River Laboratory (Beijing). Mice were housed in a 12-h light/dark cycle at 20 – 24 °C and 40 – 60% humidity. All animals involved in the study were cared for in accordance with the guidelines established by the Biomedical Research Ethics Committee of Agricultural Genomics Institute in Shenzhen, Chinese Academy of Agricultural Sciences.

Cell culture

The mouse embryonic fibroblasts, A9, $A9^{td}$, $A9^{CN}$, $A9^{CN}H1^{GFP}$ and $A9^{td}H1^{GFP}$ cell lines were grown in Dulbecco's modified Eagle's medium (DMEM; YEASEN) supplemented with 10% fetal bovine serum (FBS; Biological Industries).

The CHO, CHO^{td}, CHO^{CN}, $CHO^{CN}DBA^{GFP}$ and $CHO^{td}DBA^{GFP}$ cell lines were maintained in Ham's

F-12 nutrient mixture (Gibco) containing 10% FBS (Gibco).

C57BL/6 and DBA/2 mESCs were cultured on irradiated mouse embryonic fibroblasts. Cells were passaged every 3 - 4 days with Trypsin (Gibco) at a split ratio of 1:8 - 1:10. The components of the mouse ESC culture medium (2iL) are: Dulbecco's modified Eagle medium (DMEM) (Millipore), 15% FBS (Gibco), 1 × minimal essential medium (MEM) nonessential amino acids solution (Gibco), 1 × GlutaMAX (Gibco), 1 × Nucleosides (Gibco), 1 × β-mercaptoethanol (Gibco), 1 μM PD0325901 (Selleck), 3 μM CHIR99021 (Selleck), and 1000 units/mL mouse LIF (Millipore).

Human ES cell line H1 (WA01, Passages 25-45) were kindly provided by Prof Xiaoqing Zhang (Tongji University, Shanghai, China). H1 ESCs were cultured on Matrigel (Corning)-coated dishes in ncTarget (nuwacell) and passaged every 5 – 7 days through dispase (Gibco) digestion.

Mycoplasma contamination test was performed weekly.

In vitro transcription of Cas9 mRNA and sgRNAs

To prepare Cas9 mRNA, the T7 promoter sequence was added to the Cas9 coding region by PCR amplification of px260 (Addgene, 42229) using the primer pair listed in Table S2A. The T7-Cas9 PCR product was purified using Gel Extraction Kit (Omega) and used as the template for in vitro transcription (IVT) of Cas9 mRNA using the mMESSAGE mMACHINE T7 kit (Life Technologies). To prepare sgRNAs, the T7 promoter sequence was added to the sgRNA template by PCR amplification of px330 (Addgene, 42230) using the primer pair listed in Table S2A. The T7-sgRNA PCR product was purified using Gel Extraction Kit (Omega) and used as the template for IVT of sgRNAs using the MEGAshortscript T7 kit (Life Technologies). Both the Cas9 mRNA and sgRNAs were purified using the MEGAclear kit (Life Technologies) and eluted with elution buffer according to the standard protocol.

Microinjection of mRNAs into zygotes

Super ovulated B6D2F1 female mice (8 weeks old) were mated with B6D2F1 male mice (2 – 6 months old). Zygotes were collected at E0.5 (the presence of a virginal plug was defined as E0.5) in M2 medium (Millipore) and cultured in KSOM+AA with D-Glucose (Millipore). The mixture of Cas9 mRNA (100 ng/μl) and sgRNAs (100 ng/μl) was injected into the cytoplasm of zygotes with well recognized two pronuclei in a droplet of M2 medium containing 5 μg/ml cytochalasin B (CB, Sigma-Aldrich) using a FemtoJet microinjector (Eppendorf) with continuous flow settings.

Derivation of mESCs

Mouse blastocysts from C57BL/6 and DBA/2 were used for mESCs derivation. In brief, zona pellucida was removed with Tyrode's solution (Sigma-Aldrich), and each blastocyst was transferred into a 96-well plate and cultured on mouse embryonic fibroblasts (MEFs) with 2iL medium. After 5 – 7 days in culture, the outgrowths of blastocysts were disaggregated and replated onto newly prepared MEFs.

Plasmid construction and genome editing

mCAG-Puro-GFP plasmid for generation of DBA-puro-GFP cell line was comprised of homology arms span intergenic region between *Uty* and *Ddx3y* (chrY: 1259028-1260324 GRCm39/mm39 mouse assembly) and a CAG-puro-GFP cassette. mCAG-Puro-GFP plasmid, plasmids encoding Cas9 and sgRNA1 were transfected into dissociated DBA/2 mouse ESCs using Lipofectamine 3000

(Thermo Fisher Scientific) following the protocol recommended by the manufacturer.

hCAG-Puro-GFP plasmid for generation of H1-puro-GFP cell line contains homology arms span intergenic region between *DDX3Y* and *UTY* (chrY: 13095712-13096644 GRCh38/hg38 human assembly) and a CAG-puro-GFP cassette. hCAG-Puro-GFP plasmid was electroporated into human ES cell line H1 (WA01) with Cas9 plasmid and sgRNA4 as described[47].

48 h post-transfection, both DBA/2 and H1 ESCs were treated with 1 μg/mL puromycin (InvivoGen). Drug-resistant colonies were manually picked between 5 and 7 days and further expanded clonally.

To generate CHO^{td} and $A9^{td}$ cell lines, PBL-CAG-tdTomato-PBR and CMV-PBase were introduced into CHO and A9 cells with Lipofectamine 3000 (Thermo Fisher Scientific) using the manufacturer's instructions, according to a previous report[48]. 5 – 7 days after transfection, cells were sorted out by BD FACS Aria II and cultured into independent cell lines.

The mCherry-NLS plasmid containing three copies of the SV40 LT NLS as reported[49]. To generate CHO^{CN} cell line, CHO cells were transfected with pmCherry–NLS using Lipofectamine 3000 (Thermo Fisher Scientific) and isolated through cell sorting.

Genotyping

Genomic DNA of mouse blastocysts and ESCs were extracted using lysis buffer containing proteinase K (Vazyme). Genomic DNA of mouse tissues were extracted using DNeasy Blood & Tissue Kit (QIAGEN) and diluted using ddH_2O. Genomic PCRs were performed using 2 × Hieff Canace® Plus PCR Master Mix (YEASEN). The PCR products were examined by 1.5% agarose gel electrophoresis and then sent for Sanger sequencing. Primer sequences were listed in Table S2B.

Generation of $CHO^{td}DBA^{GFP}$ and $A9^{td}H1^{GFP}$ cells

To induce cell-fusion, equal numbers of CHO^{td} (or $A9^{td}$) and DBA-puro-GFP mESCs (or H1-puro-GFP hESCs) were mixed in presence of polyethylene glycol (PEG) (Roche) as directed by the manufacturer's instructions, according to a previous report[50]. The cell fusion mixtures were further cultured under standard conditions for maintenance as described above. 5 – 7 days after PEG treatment, cells exhibiting dual-positive fluorescence for both GFP and tdTomato were isolated through cell sorting. The sorted single cells were cultured into independent hybrid cell lines.

Micro-cell Mediated Chromosome Transfer (MMCT)

MMCT was performed as described[51,52]. In brief, $CHO^{td}DBA^{GFP}$ or $A9^{td}H1^{GFP}$ cells were treated with Demecolcine solution (Sigma-Aldrich) (75 ng/mL) for 72 h to induce micronucleation. Then, cells were harvested via trypsinization, washed, and treated with Latrunculin B (0.2 μM for $CHO^{td}DBA^{GFP}$; 10μM for $A9^{td}H1^{GFP}$) to disrupt cytoskeletal integrity. Microcells were isolated by Percoll gradient centrifugation (19,000 rpm, 34°C, 80 min), followed by sequential filtration through polycarbonate membranes (8, 5, and 3 μm). Purified microcells were resuspended in ice-cold cell fusion buffer (CFB).

C57BL/6 mESCs were trypsinized, adjusted to a concentration of 2 x 10^5 cells/25 μl, and mixed with microcells in CFB. HVJ-E suspension (10 μL) was added to the mixture, incubated on ice for 5 min, and fusion was triggered at 37°C for 15 min. Post-fusion, cells were cultured in 2iL medium. Puromycin selection (1 μg/mL) was performed 48 h after microcell fusion, and puro-resistant colonies were picked after 7 to 10 days.

Tetraploid compensation

For preparation of tetraploid embryos, super ovulated B6D2F1 females (8 weeks old) were mated with B6D2F1 males (2 – 6 months old). Zygotes were collected 22-24 hours after hCG injection. After 24 hr culture, E1.5 embryos at the two-cell stage were placed in the microdroplets containing 0.3 M Mannitol with 0.3% bovine serum albumin (BSA, Sigma-Aldrich) and fused with Electro Cell Fusion CFB16-HB instrument (BEX Ltd., Japan) with 0.1 cm Micro fusion slide (BTX 450-1). At first alternating current with 15 V was applied for 15 s to turn the two-cell stage embryos into the right position for fusion. After embryos had reached this position (cleaving line parallel to the electrodes), fusion pulses were started (direct current, 100 V). Time between the fusion pulses was 40 µs. The number of pulses was 2. After pulsation the embryos were washed twice immediately in KSOM+AA with D-Glucose (Millipore) and were incubated at 37°C under 5% CO_2 for 1h. The fused embryos were washed 6-8 times in KSOM+AA with D-Glucose (Millipore) and were incubated at 37°C under 5% CO_2.

For tetraploid compensation, ES cells were aggregated and cultured with denuded 4-cell stage mouse tetraploid embryos. In detail, clumps of loosely connected ES cells (15 – 20 cells in each) from short trypsin-treated Day2 ES cultures were transferred into microdroplets of KSOM+AA with D-Glucose under mineral oil. Each clump was placed in a depression in the microdroplet. Meanwhile, 30-50 embryos were briefly incubated in Tyrode's solution until dissolution of their zona pellucida. Two embryos were placed on one ES clump. All aggregates were assembled in this manner and cultured overnight at 37°C under 5% CO_2.

For mouse embryo transfer, ICR female mice (8 weeks old) in the stage of estrus were selected as recipients and mated with vasectomized ICR males (3 – 12 months old) overnight to induce pseudopregnancy. Approximately 15 – 20 blastocysts were transferred into the uterine horn of a 2.5 dpc pseudo pregnant recipient.

Immunofluorescence

Cells were fixed with 4% paraformaldehyde (PFA) for 10 min at room temperature, washed three times with PBS, permeabilized and blocked with 0.1% Triton X-100 with 10% normal donkey serum (Jackson ImmunoResearch Laboratories) in PBS for 1 h. Staining with primary antibodies were performed overnight at 4 °C in 10% normal donkey serum and 0.1% Triton X-100. After three washes in PBS, secondary antibodies and DAPI were applied for 1 h at room temperature. Coverslips were then mounted on glass slides using SlowFade Diamond Antifade Mountant (Invitrogen). The following primary antibodies were used: anti-Oct3/4 (mouse monoclonal, 1:100; sc-5729, Santa Cruz), anti-Sox2 (Rabbit polyclonal, 1:100; AB5603, Millipore), anti-SSEA1 (mouse monoclonal, 1:100; MAB4301, Millipore), Anti-phosphorylated histone H2AX (Ser139) (mouse monoclonal, 1:1000; 05-636, Millipore).

Mouse tissues were fixed with 4% PFA for 24 h at 4°C, dehydrated in 15% and 30% sucrose overnight at 4°C respectively until the tissues sank to the bottom of the tube, then embedded in O.C.T. compound at -30°C and stored at -80°C until further processing. Frozen tissues were cut on a cryostat (Leica CM1950) into 8 µm-thick sections for immunostaining. The slides were washed three times with PBS. After permeabilization and blocking with 0.1% Triton X-100 with 10% normal donkey serum in PBS for 1 h at room temperature. Slides were incubated with primary antibodies overnight at 4°C, secondary antibodies for 1 h at room temperature, and finally DAPI. The images of stained slides were taken by Nikon A1 confocal microscope. All quantitative

547 analysis of immunostained sections were carried out using ImageJ. The following primary
548 antibodies were used: Anti-mouse CD45 (Rat monoclonal, 1:100; 550539, BD Bioscience), Anti-
549 mouse CD68 (Rat monoclonal, 1:100; MCA1957T, BIO-RAD).
550
551 **Metaphase spread preparation**
552 Mouse ES cells were treated for 1.5 – 2 h with 200 ng/ml Demecolcine solution (Sigma-Aldrich),
553 harvested by trypsinization and centrifugation. Cell pellets were resuspended in 200 µl PBS
554 followed by adding 2 ml of hypotonic 75 mM KCl/PBS (7:3) solution dropwise while gently
555 vortexing, incubated for 10 min at 37 °C water bath and fixed using freshly prepared, ice-cold
556 methanol/acetic acid (3:1). Cells were subsequently dropped onto slides and air dried for further
557 processing.
558
559 **DNA fluorescence in situ hybridization (FISH)**
560 FISH probes (MetaSystems) were applied to metaphase spreads dropped onto slides. Slides were
561 sealed with a coverslip and denatured at 75°C for 2 min and incubated in a humidified chamber at
562 37°C overnight for hybridization. Slides were washed with 0.4× SSC at 72°C for 2 min and 2× SSC,
563 0.05% Tween-20 at room temperature for 30 s. Then rinsed briefly in distilled water to avoid crystal
564 formation. Slides were air-dried, stained with DAPI and mounted with SlowFade Diamond Antifade
565 Mountant (Invitrogen).
566 For immunofluorescence combined with DNA FISH (IF-FISH), the immunofluorescence procedure
567 was performed first. In detail, cell suspensions were concentrated to 1×10^6 cells per ml in PBS and
568 centrifuged onto glass slides using a Cytospin centrifuge (CenLee), fixed with 4% formaldehyde for
569 10 min, washed three times with PBS, permeabilized in 0.3% Triton X-100 in PBS for 5 min,
570 incubated in Triton Block (0.2 M glycine, 2.5% fetal bovine serum, 0.1% Triton X-100, PBS) for 1
571 h at room temperature. Staining with primary antibodies was performed overnight at 4 °C. The
572 following primary antibodies were used at the indicated dilutions in Triton Block: Anti-
573 phosphorylated histone H2AX (Ser139) (Rabbit polyclonal, 1:400; 2577, Cell Signaling
574 Technology), Anti-CENP-A (C51A7) (Rabbit monoclonal, 1:200; 2048, Cell Signaling Technology).
575 Cells were washed with 0.1% Triton X-100 in PBS, incubated with 1:1,000 dilutions of Alexa Fluor-
576 conjugated donkey anti-rabbit or donkey anti-mouse secondary antibodies (Jackson
577 ImmunoResearch Laboratories) for 1 h at room temperature, and washed with 0.1% Triton X-100
578 in PBS. Immunostained cells were fixed with freshly prepared, ice-cold methanol/acetic acid (3:1)
579 for 15 min at room temperature. Slides were rinsed with 80% ethanol and air-dried before
580 proceeding to the FISH protocol. The following FISH probes were used: XCP Y green (D-0324-
581 050-FI, Metasystem), XMP Y green (D-1421-050-FI, Metasystem), XMP X orange (D-1420-050-
582 OR, Metasystem).
583
584 **Real-time genomic DNA PCR**
585 Real-time genomic DNA PCR was performed as described[53]. In brief, genomic DNA was digested
586 with EcoRI (New England Biolabs). The *Omp* gene on mouse chr7 was selected as reference gene
587 due to no aneuploidy was detected for this chromosome in C57 XY^H mESCs (Figure 3E). To assess
588 the retention rate of the human chrY, we designed specific primers targeting exonic regions of UTY
589 gene. The primers used for qPCR are provided in Table S2C. The qPCR mixture (20 µl) contained
590 10 µl Taq Pro Universal SYBR qPCR Master Mix (Vazyme), 0.4 µl of each primer (at 10 pM), 6.5

µl of ddH2O, and 3 µl of digested genomic ESC DNA. Reaction was run on a Bio-rad CFX Opus 96 using the following cycling conditions: an initial denaturation step at 95 °C for 5 min, followed by a 39 cycles amplification step of 95 °C for 15 s, 60 °C for 15 s, and 72 °C for 15s and a final cooling step at 40 °C for 30 s.

Droplet digital PCR (ddPCR)

ddPCR was performed as described[54]. In brief, the Sod2 gene on mouse chr17 and the RPPH1 gene on human chr14 were selected as reference gene. To assess the copy number of chrY, we designed specific primers targeting puromycin. The primers and probes used for ddPCR are provided in Table S2D. Genomic DNA was digested with HindIII (New England Biolabs). The ddPCR mixture (20 µl) contained 60ng genomic DNA, 1x ddPCR Supermix for probes (Bio-Rad), 225 nM of each primer and 50 nM of each probe (one VIC-labelled probe for the reference gene assay and one 6-FAM-labelled for Y chromosome target assay). Reaction was amplified on the Bio-Rad C1000 Touch thermocycler (95 °C for 10 min, followed by 40 cycles of 94 °C for 30 s and 58 °C for 60 s, with a final step of 98 °C for 10 min). The plate containing the droplet amplicons was subsequently loaded into the QX200 Droplet Reader (Bio-Rad). The Y chromosome target was amplified in parallel with a reference gene assay, a copy number variation experiment with the reference set at 2 copies (euploid, CNV2) on the Bio-Rad QX200 ddPCR system (Bio-Rad, CA) was performed.

Whole-genome sequencing (WGS) analysis

Genomic DNA was isolated from ~1×10^6 cells or 10 – 50 mg tissues using the DNeasy Blood and Tissue Kit (QIAGEN). WGS was performed by MGI2000. The raw data were qualified by SOAPnupk (v2.1.6)[55] with default parameters. Qualified reads were mapped to the mouse genome (mm39) or combined reference genome (mm39 and the Y chromosome of T2T-CHM13 v2.0) by BWA mem (v0.7.12)[56]. Aligned sequencing reads were processed using Samtools (v1.12)[57], and duplicate reads were flagged using Sambamba (v0.8.1)[58]. Sequencing depth was calculated at 100 base pair windows using Mosdepth (v0.3.1)[59]. Control-FREEC (v11.6)[60] was used to perform copy-number variation analysis using default parameters.

To identify the genome wide variants with high confidence, we conducted single nucleotide variation and InDels calling using Mutect2 (v4.2.0).

RNA isolation and RNA-seq

Total RNA of each sample was extracted using Trizol (Invitrogen) according to the standard protocol. High-throughput mRNA sequencing was carried out using Illumina Novaseq 6000 and ~22 million reads were produced for each library. FastQC (v0.11.8) and Trimmomatic (v0.39)[61] were used for quality control. Qualified reads were mapped to the mouse genome (mm39) or combined reference genome (mm39 and the Y chromosome of T2T-CHM13 v2.0) by STAR (v2.7.10a)[62] with two pass models. Differentially expressed genes were analyzed using DESeq2.

Differentially expressed genes (DEGs) analysis

A comparative analysis was conducted on the gene expression patterns in 8 tissues procured from six C57 XY^H GFP^+ mice and five male C57BL/6 mice aged P1 to P15. Initially, marker genes were identified within tissues of male C57BL/6 mice by selecting those with a log2(Fold-change) exceeding 0.25 and adjusted p-value less than 0.05. Subsequently, the expression patterns of these

identified genes were examined in tissues from both male C57BL/6 mice and C57 XY^{H} GFP^{+} mice. The DEGs of each tissue was visualized in Table S3.

Gene function annotation of differentially expressed genes

We calculated differentially expressed genes (DEGs) for each cell type between the C57 XY^{H} GFP^{+} mice and male C57BL/6 mice. Genes with adjusted p-values less than 0.05 and absolute log2(Fold-Change) greater than 0.25 were selected as significantly different genes within each tissue. Then, functional annotation of differentially expressed genes in each tissue was performed using the enrichGO function from the clusterProfiler (v4.14.0)[63]. Clustered GO terms with significantly low p-values (<0.05) and a gene count greater than or equal to 5 were considered as functionally enriched entries. The GO analysis result of each tissue was visualized in Table S4.

Statistics

All values are presented as mean ± SEM. from at least three independent experiments. Unpaired Student's *t*-test (two tailed), Repeated Measures ANOVA and log-rank test were used to evaluate statistical significance (*$P < 0.05$, **$P < 0.01$, ***$P < 0.001$, ****$P < 0.0001$). Randomization was used in all experiments. Data visualization and analysis were performed using GraphPad Prism version 9.0 (GraphPad Software) and Microsoft Excel (Microsoft 365).

Acknowledgments

We thank Dr. Peter Ly for guidance in establishing the IF-FISH protocol. We thank all colleagues in Zuo's laboratory for their technical assistance and helpful discussions. The study was financially supported by the National Natural Science Foundation of China (Grant number 32371549, 32101223 and 82101872), the Innovation Program of Chinese Academy of Agricultural Sciences (CAAS-CSIAF-202401, CAAS-BRC-AFIS-2025-03, CAAS-SCAB-202301).

Author Contributions

L.S., J.W., and E.Z. designed experiments. L.S. derived C57 XY^D and C57 XY^H mESCs. X.Y. and C.Z. performed in vitro transcription and genotyping and performed microinjection. X.Y. performed tetraploid compensation. L.S., X.Y. and C.Z. performed FISH and immunofluorescence analysis. L.S. and M.W. performed data analysis. L.S. and E.Z. wrote the manuscript. J.W. and E.Z. supervised the project.

Data Availability

The raw sequence data are available from the National Center for Biotechnology Information Sequence Read Archive database under the accession code PRJNA1259728. All raw sequence data are also available from the China National GenBank DataBase under accession number CNP0007331.

Reference

1 Nadeau, J. H., Singer, J. B., Matin, A. & Lander, E. S. Analysing complex genetic traits with chromosome substitution strains. *Nature Genetics* **24**, 221-225, doi:10.1038/73427 (2000).

2 Wijnen, C. L. *et al.* A complete chromosome substitution mapping panel reveals genome-wide epistasis in Arabidopsis. *Heredity* **133**, 198-205, doi:10.1038/s41437-024-00705-1 (2024).

3 Shao, H. *et al.* Genetic architecture of complex traits: Large phenotypic effects and pervasive epistasis. *Proceedings of the National Academy of Sciences of the United States of America* **105**, 19910-19914, doi:10.1073/pnas.0810388105 (2008).

4 Singer, J. B. *et al.* Genetic dissection of complex traits with chromosome substitution strains of mice. *Science* **304**, 445-448, doi:10.1126/science.1093139 (2004).

5 Miller, A. K. *et al.* A Novel Mapping Strategy Utilizing Mouse Chromosome Substitution Strains Identifies Multiple Epistatic Interactions That Regulate Complex Traits. *G3-Genes Genomes Genetics* **10**, 4553-4563, doi:10.1534/g3.120.401824 (2020).

6 Kazuki, Y. & Oshimura, M. Human Artificial Chromosomes for Gene Delivery and the Development of Animal Models. *Molecular Therapy* **19**, 1591-1601, doi:10.1038/mt.2011.136 (2011).

7 Bellaloui, N. *et al.* Effects of Interspecific Chromosome Substitution in Upland Cotton on Cottonseed Macronutrients. *Plants-Basel* **10**,

doi:10.3390/plants10061158 (2021).

8 Xu, J. *et al.* Developing high throughput genotyped chromosome segment substitution lines based on population whole-genome re-sequencing in rice (Oryza sativa L.). *Bmc Genomics* **11**, doi:10.1186/1471-2164-11-656 (2010).

9 Flint, J., Valdar, W., Shifman, S. & Mott, R. Strategies for mapping and cloning quantitative trait genes in rodents. *Nature Reviews Genetics* **6**, 271-286, doi:10.1038/nrg1576 (2005).

10 Kalitsis, P. & Choo, K. H. A. The evolutionary life cycle of the resilient centromere. *Chromosoma* **121**, 327-340, doi:10.1007/s00412-012-0369-6 (2012).

11 Henikoff, S., Ahmad, K. & Malik, H. S. The centromere paradox: Stable inheritance with rapidly evolving DNA. *Science* **293**, 1098-1102, doi:10.1126/science.1062939 (2001).

12 Logsdon, G. A. & Eichler, E. E. Chromosome components central to cell division evolve rapidly. *Nature*, doi:10.1038/d41586-024-02523-1 (2024).

13 Zuo, E. *et al.* CRISPR/Cas9-mediated targeted chromosome elimination. *Genome Biology* **18**, doi:10.1186/s13059-017-1354-4 (2017).

14 Hashizume, R. *et al.* Trisomic rescue via allele-specific multiple chromosome cleavage using CRISPR-Cas9 in trisomy 21 cells. *Pnas Nexus* **4**, doi:10.1093/pnasnexus/pgaf022 (2025).

15 Tsuchida, C. A. *et al.* Mitigation of chromosome loss in clinical CRISPR-Cas9-engineered T cells. *Cell* **186**, 4567-+, doi:10.1016/j.cell.2023.08.041 (2023).

16 Sano, S. *et al.* Hematopoietic loss of Y chromosome leads to cardiac fibrosis and heart failure mortality. *Science* **377**, 292-297, doi:10.1126/science.abn3100 (2022).

17 Suzuki, T., Kazuki, Y., Hara, T. & Oshimura, M. Current advances in microcell-mediated chromosome transfer technology and its applications. *Experimental Cell Research* **390**, doi:10.1016/j.yexcr.2020.111915 (2020).

18 Kazuki, K. *et al.* Highly stable maintenance of a mouse artificial chromosome in human cells and mice. *Biochemical and Biophysical Research Communications* **442**, 44-50, doi:10.1016/j.bbrc.2013.10.171 (2013).

19 Takiguchi, M. *et al.* A Novel and Stable Mouse Artificial Chromosome Vector. *Acs Synthetic Biology* **3**, 903-914, doi:10.1021/sb3000723 (2014).

20 O'Doherty, A. *et al.* An aneuploid mouse strain carrying human chromosome 21 with Down syndrome phenotypes. *Science* **309**, 2033-2037, doi:10.1126/science.1114535 (2005).

21 Crasta, K. *et al.* DNA breaks and chromosome pulverization from errors in mitosis. *Nature* **482**, 53-U70, doi:10.1038/nature10802 (2012).

22 Liu, S. *et al.* Nuclear envelope assembly defects link mitotic errors to chromothripsis. *Nature* **561**, 551-+, doi:10.1038/s41586-018-0534-z (2018).

23 Zhang, C.-Z. *et al.* Chromothripsis from DNA damage in micronuclei. *Nature* **522**, 179-+, doi:10.1038/nature14493 (2015).

24 Wilhelm, D., Palmer, S. & Koopman, P. Sex determination and gonadal

development in mammals. *Physiological Reviews* **87**, 1-28, doi:10.1152/physrev.00009.2006 (2007).

25 Godfrey, A. K. *et al.* Quantitative analysis of Y-Chromosome gene expression across 36 human tissues. *Genome Research* **30**, 860-873, doi:10.1101/gr.261248.120 (2020).

26 Ly, P. *et al.* Selective Y centromere inactivation triggers chromosome shattering in micronuclei and repair by non-homologous end joining. *Nature Cell Biology* **19**, 68-75, doi:10.1038/ncb3450 (2017).

27 Fachinetti, D. *et al.* DNA Sequence-Specific Binding of CENP-B Enhances the Fidelity of Human Centromere Function. *Developmental Cell* **33**, 314-327, doi:10.1016/j.devcel.2015.03.020 (2015).

28 Earnshaw, W. C. *et al.* Molecular cloning of cDNA for CENP-B, the major human centromere autoantigen. *The Journal of cell biology* **104**, 817-829, doi:10.1083/jcb.104.4.817 (1987).

29 McKinley, K. L. & Cheeseman, I. M. The molecular basis for centromere identity and function. *Nature Reviews Molecular Cell Biology* **17**, doi:10.1038/nrm.2015.5 (2016).

30 Malik, H. S. & Henikoff, S. Adaptive evolution of cid, a centromere-specific histone in drosophila. *Genetics* **157**, 1293-1298 (2001).

31 Maheshwari, S. *et al.* Naturally Occurring Differences in CENH3 Affect Chromosome Segregation in Zygotic Mitosis of Hybrids. *Plos Genetics* **11**, doi:10.1371/journal.pgen.1004970 (2015).

32 Rattner, J. B. The structure of the mammalian centromere. *BioEssays : news and reviews in molecular, cellular and developmental biology* **13**, 51-56, doi:10.1002/bies.950130202 (1991).

33 Stirpe, A. & Heun, P. The ins and outs of CENP-A: Chromatin dynamics of the centromere-specific histone. *Seminars in Cell & Developmental Biology* **135**, 24-34, doi:10.1016/j.semcdb.2022.04.003 (2023).

34 Kitaoka, M., Smith, O. K., Straight, A. F. & Heald, R. Molecular conflicts disrupting centromere maintenance contribute to Xenopus hybrid inviability. *Current Biology* **32**, 3939-+, doi:10.1016/j.cub.2022.07.037 (2022).

35 Wu, Z., Qu, J. & Liu, G.-H. Roles of chromatin and genome instability in cellular senescence and their relevance to ageing and related diseases. *Nature Reviews Molecular Cell Biology* **25**, 979-1000, doi:10.1038/s41580-024-00775-3 (2024).

36 Zhao, Y., Simon, M., Seluanov, A. & Gorbunova, V. DNA damage and repair in age-related inflammation. *Nature Reviews Immunology* **23**, 75-89, doi:10.1038/s41577-022-00751-y (2023).

37 Pezone, A. *et al.* Inflammation and DNA damage: cause, effect or both. *Nature Reviews Rheumatology* **19**, 200-211, doi:10.1038/s41584-022-00905-1 (2023).

38 Goverman, J. M. Immune tolerance in multiple sclerosis. *Immunological reviews* **241**, 228-240, doi:10.1111/j.1600-065X.2011.01016.x (2011).

39 Chen, X. *et al.* Microglia-mediated T cell infiltration drives neurodegeneration in tauopathy. *Nature* **615**, 668-677, doi:10.1038/s41586-023-05788-0 (2023).

40 Li, Z. K. *et al.* Adult bi-paternal offspring generated through direct modification

of imprinted genes in mammals. *Cell stem cell* **32**, 361-374.e366, doi:10.1016/j.stem.2025.01.005 (2025).

41 Suzuki, N., Nishii, K., Okazaki, T. & Ikeno, M. Human artificial chromosomes constructed using the bottom-up strategy are stably maintained in mitosis and efficiently transmissible to progeny mice. *Journal of Biological Chemistry* **281**, 26615-26623, doi:10.1074/jbc.M603053200 (2006).

42 Carroll, C. W., Milks, K. J. & Straight, A. F. Dual recognition of CENP-A nucleosomes is required for centromere assembly. *Journal of Cell Biology* **189**, 1143-1155, doi:10.1083/jcb.201001013 (2010).

43 de Jong, G., Telenius, A., Vanderbyl, S., Meitz, A. & Drayer, J. Efficient in-vitro transfer of a 60-Mb mammalian artificial chromosome into murine and hamster cells using cationic lipids and dendrimers. *Chromosome Research* **9**, 475-485, doi:10.1023/a:1011680529073 (2001).

44 Suzuki, N., Itou, T., Hasegawa, Y., Okazaki, T. & Ikeno, M. Cell to cell transfer of the chromatin-packaged human β-globin gene cluster. *Nucleic Acids Research* **38**, doi:10.1093/nar/gkp1168 (2010).

45 Klobutcher, L. A., Miller, C. L. & Ruddle, F. H. Chromosome-mediated gene transfer results in two classes of unstable transformants. *Proc Natl Acad Sci U S A* **77**, 3610-3614, doi:10.1073/pnas.77.6.3610 (1980).

46 Petris, G. *et al.* High-fidelity human chromosome transfer and elimination. *Science* **390**, 1038-1043, doi:10.1126/science.adv9797 (2025).

47 Chi, L. *et al.* The Dorsoventral Patterning of Human Forebrain Follows an Activation/Transformation Model. *Cerebral Cortex* **27**, 2941-2954, doi:10.1093/cercor/bhw152 (2017).

48 Huang, J. *et al.* Generation of rat forebrain tissues in mice. *Cell* **187**, doi:10.1016/j.cell.2024.03.017 (2024).

49 Micutkova, L. *et al.* Analysis of the cellular uptake and nuclear delivery of insulin-like growth factor binding protein-3 in human osteosarcoma cells. *International Journal of Cancer* **130**, 1544-1557, doi:10.1002/ijc.26149 (2012).

50 Cowan, C. A., Atienza, J., Melton, D. A. & Eggan, K. Nuclear reprogramming of somatic cells after fusion with human embryonic stem cells. *Science* **309**, 1369-1373, doi:10.1126/science.1116447 (2005).

51 Liskovykh, M., Lee, N. C. O., Larionov, V. & Kouprina, N. Moving toward a higher efficiency of microcell-mediated chromosome transfer. *Molecular Therapy-Methods & Clinical Development* **3**, doi:10.1038/mtm.2016.43 (2016).

52 Sanford, J. A. & Stubblefield, E. General protocol for microcell-mediated chromosome transfer. *Somatic cell and molecular genetics* **13**, 279-284, doi:10.1007/bf01535210 (1987).

53 D'Hulst, C., Parvanova, I., Tomoiaga, D., Sapar, M. L. & Feinstein, P. Fast Quantitative Real-Time PCR-Based Screening for Common Chromosomal Aneuploidies in Mouse Embryonic Stem Cells. *Stem Cell Reports* **1**, 350-359, doi:10.1016/j.stemcr.2013.08.003 (2013).

54 Codner, G. F. *et al.* Aneuploidy screening of embryonic stem cell clones by metaphase karyotyping and droplet digital polymerase chain reaction. *Bmc Cell*

Biology **17**, doi:10.1186/s12860-016-0108-6 (2016).

55 Chen, Y. *et al.* SOAPnuke: a MapReduce acceleration-supported software for integrated quality control and preprocessing of high-throughput sequencing data. *Gigascience* **7**, doi:10.1093/gigascience/gix120 (2017).

56 Li, H. & Durbin, R. Fast and accurate short read alignment with Burrows-Wheeler transform. *Bioinformatics* **25**, 1754-1760, doi:10.1093/bioinformatics/btp324 (2009).

57 Danecek, P. *et al.* Twelve years of SAMtools and BCFtools. *Gigascience* **10**, doi:10.1093/gigascience/giab008 (2021).

58 Tarasov, A., Vilella, A. J., Cuppen, E., Nijman, I. J. & Prins, P. Sambamba: fast processing of NGS alignment formats. *Bioinformatics* **31**, 2032-2034, doi:10.1093/bioinformatics/btv098 (2015).

59 Pedersen, B. S. & Quinlan, A. R. Mosdepth: quick coverage calculation for genomes and exomes. *Bioinformatics* **34**, 867-868, doi:10.1093/bioinformatics/btx699 (2018).

60 Boeva, V. *et al.* Control-FREEC: a tool for assessing copy number and allelic content using next-generation sequencing data. *Bioinformatics* **28**, 423-425, doi:10.1093/bioinformatics/btr670 (2012).

61 Bolger, A. M., Lohse, M. & Usadel, B. Trimmomatic: a flexible trimmer for Illumina sequence data. *Bioinformatics* **30**, 2114-2120, doi:10.1093/bioinformatics/btu170 (2014).

62 Dobin, A. *et al.* STAR: ultrafast universal RNA-seq aligner. *Bioinformatics* **29**, 15-21, doi:10.1093/bioinformatics/bts635 (2013).

63 Wu, T. *et al.* clusterProfiler 4.0: A universal enrichment tool for interpreting omics data. *Innovation* **2**, doi:10.1016/j.xinn.2021.100141 (2021).

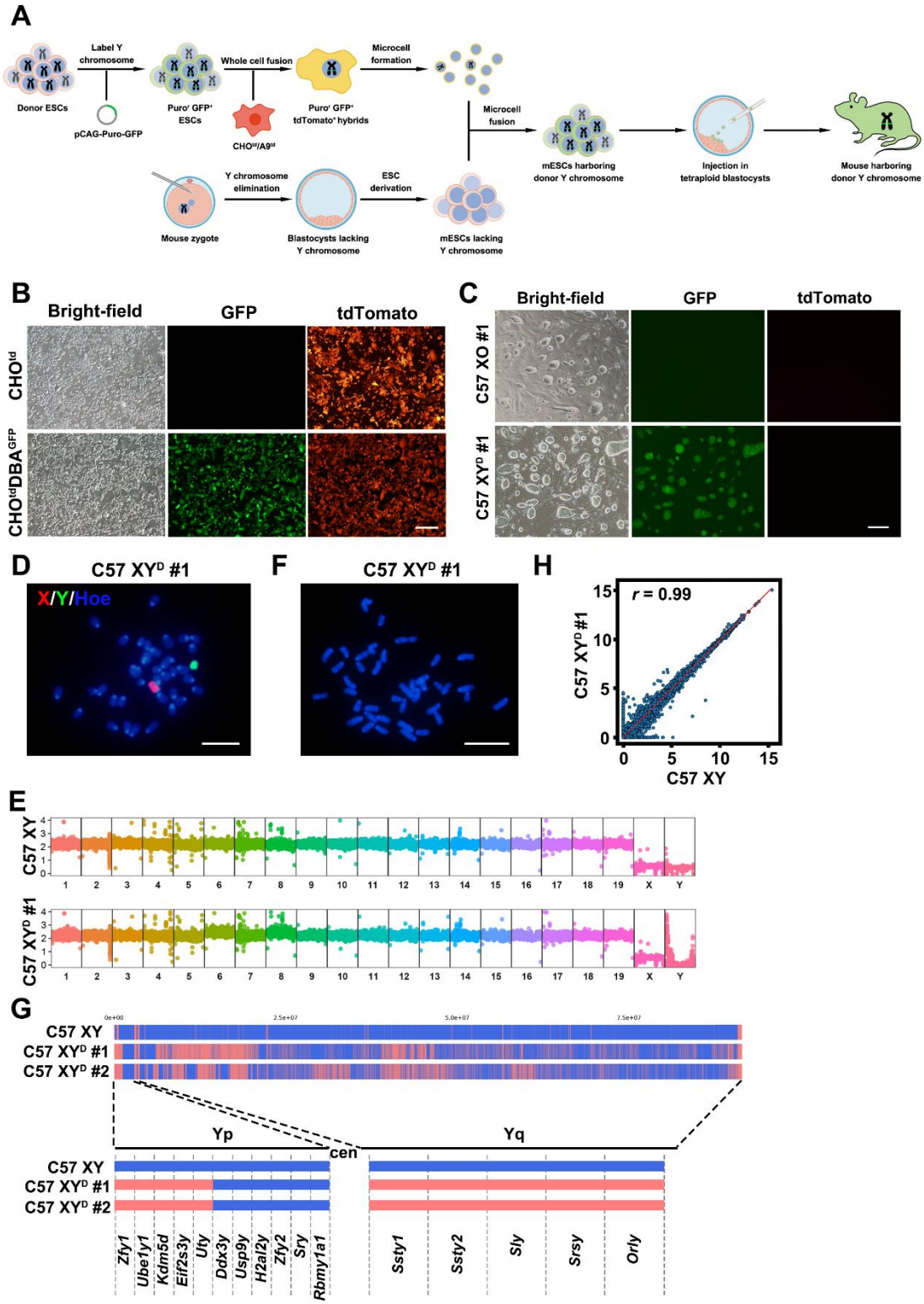

Figure 1 Derivation of euploid C57 XY^D mESCs through mouse Y chromosome replacement

A. Stepwise strategy to introduce exogenous chromosomes without inducing aneuploidy.

B. Morphology of CHO^{td} cell line and CHO^{td}DBA^{GFP} cell line. CHO^{td}DBA^{GFP} cells harbor both the DBA-puro-GFP-originated GFP marker and the CHO^{td}-originated tdTomato marker. Scale bar, 500 μm.

C. Morphology of C57 XO #1 and C57 XY^D #1 ESCs. C57 XY^D #1 cells exclusively harbor the

DBA-puro-GFP-originated GFP marker, lacking the CHO^{td}-originated tdTomato marker. Scale bar, 500 μm.

D. Representative DNA-FISH analysis of C57 XY^D #1 ESCs. Green, whole-chromosome probe for mouse Y chromosome; red, whole-chromosome probe for mouse X chromosome; blue, Hoechst-labeled DNA. Scale bar, 10 μm.

E. WGS analysis confirmed the presence of chrY in the C57 XY^D #1 ESC line. C57 XY, male C57BL/6 ESC line; Vertical axis, copy number; horizontal axis, chromosome number.

F. Karyotyping of C57 XY^D #1 ESCs showed 40 chromosomes. Scale bar, 10 μm.

G. Mouse chrY content in male C57BL/6 (C57 XY), C57 XY^D #1 and C57 XY^D #2 ESC line. Top, WGS coverage profiles of the mouse chrY across three cell lines (C57 XY, C57 XY^D #1, and C57 XY^D #2) are displayed. The genomic positions (0.0 - 7.5 × 10^7 bp) along the chrY are indicated at the top. Blue regions represent sequencing read coverage, confirming the presence of Y chromosomal DNA, while red regions denote coverage gaps. Bottom, cell line names are shown on the left and vertical bars that indicate the presence of the mouse chrY markers listed at the bottom. Markers are shown in order but are not spaced relative to their distance apart on chrY. Blue denotes the presence of the marker, red denotes a negative score, i.e., the marker was not present. Yp, the short arm of chrY; Yq, the long arm of chrY; cen, centromere.

H. Comparison of gene expression values between C57 XY^D #1 ESCs and C57 XY ESCs. C57 XY, male C57BL/6 ESC line.

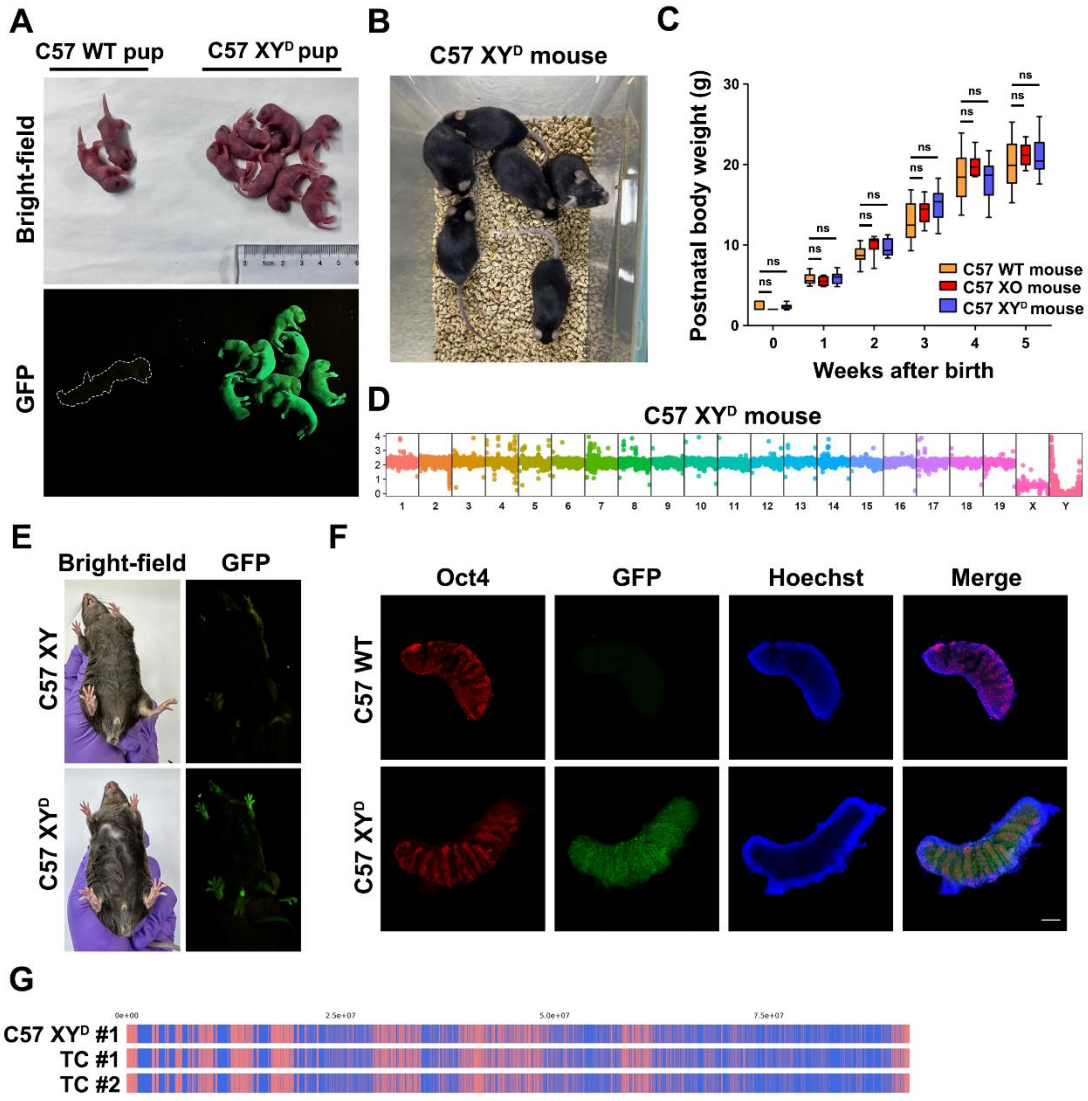

Figure 2 Production of viable mice that carry intraspecies Y chromosome

A. Generation of full-term C57 XY^D pups. Photographs are shown in the top row, and images for GFP signals are shown in the bottom row.

B. Adult C57 XY^D mice.

C. Growth curves of wild-type C57BL/6 (n = 8), C57 XO (n = 6), and C57 XY^D (n = 8) mice. ns, no significance.

D. WGS analysis confirmed the presence of mouse chrY in the C57 XY^D mouse. Vertical axis, copy number; horizontal axis, chromosome number.

E. Adult C57 XY^D mouse showed male primary sex characteristics. The images for GFP signals are shown on the right. C57 XY mouse, male C57BL/6 mouse.

F. Immunofluorescence staining of E12.5 male C57BL/6 and C57 XY^D mouse genital ridges was shown, with Oct4 used as a marker for gonocytes. Scale bar, 200 μm.

G. WGS coverage profiles of the mouse chrY are displayed. The genomic positions (0.0–7.5 × 10^7 bp) along the chrY are indicated at the top. Blue regions represent sequencing read coverage, confirming the presence of Y chromosomal DNA, while red regions denote coverage gaps. C57 XY^D #1, C57 XY^D #1 mESCs; TC #1, C57 XY^D mice #1; TC #2, C57 XY^D mice #2.

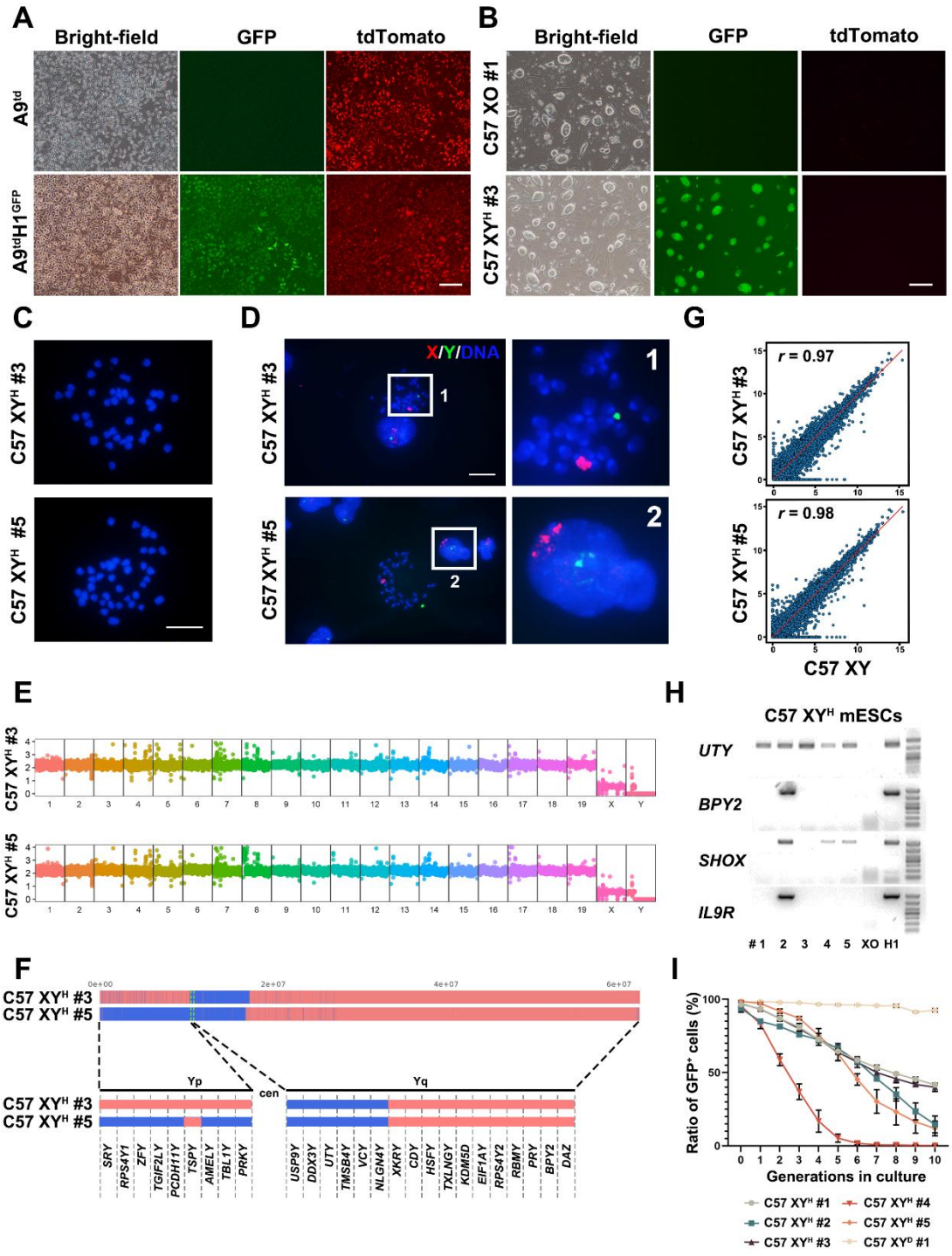

Figure 3 Derivation of euploid C57 XY^{H} mESCs and evaluation of human chrY stability in vitro

A. Morphology of A9^{td} cell line and A9^{td}H1^{GFP} cell line. A9^{td}H1^{GFP} cells harbor both the H1-puro-GFP-originated GFP marker and the A9^{td}-originated tdTomato marker. Scale bar, 500 μm.

B. Morphology of C57 XO #1 and C57 XY^{H} #3 ESCs. C57 XY^{H} #3 cells exclusively harbor the H1-puro-GFP-originated GFP marker, lacking the A9^{td}-originated tdTomato marker. Scale bar, 500 μm.

C. Karyotyping of C57 XY^{H} #3 and C57 XY^{H} #5 ESCs showed 40 chromosomes. Scale bar, 10

μm.

D. Representative DNA-FISH analysis of C57 XY^H #3 and C57 XY^H #5 ESCs. Green, whole-chromosome probe for human Y chromosome; red, whole-chromosome probe for mouse X chromosome; blue, Hoechst-labeled DNA. Scale bar, 10 μm.

E. WGS analysis confirmed the presence of human chrY in the C57 XY^H #3 and C57 XY^H #5 ESCs. Vertical axis, copy number; horizontal axis, chromosome number.

F. Human chrY content in C57 XY^H #3 and C57 XY^H #5 ESC line. Top, WGS coverage profiles of the chrY across two cell lines (C57 XY^H #3 and C57 XY^H #5) are displayed. The genomic positions (0.0 - 6×10^7 bp) along human chrY are indicated at the top. Blue regions represent sequencing read coverage, confirming the presence of Y chromosomal DNA, while red regions denote coverage gaps. Bottom, cell line names are shown on the left and vertical bars that indicate the presence of the human chrY markers listed at the bottom. Markers are shown in order but are not spaced relative to their distance apart on chrY. Blue denotes the presence of the marker, red denotes a negative score, i.e., the marker was not present. Yp, the short arm of chrY; Yq, the long arm of chrY; cen, centromere.

G. Comparative analysis of gene expression profiles between C57 XY^H #3 and C57 XY^H #5 ESCs relative to male C57 ESCs (C57 XY).

H. Genomic DNA PCR results of human chrY-specific genes (*UTY*, *BPY2*, *SHOX*, *IL9R*) in seven cell lines: C57 XY^H #1 – 5 (#1 – 5), C57 XO (XO), and human ESC H1 (H1). C57 XO served as a negative control (no human chrY), while H1 served as a positive control (intact human chrY). Variations of PCR results indicated distinct human chrY fragments retained in each C57 XY^H line.

I. Flow cytometry showed the ratio of GFP^+ cells after serial culture without selection pressure in C57 XY^H #1 – 5 and C57 XY^D #1.

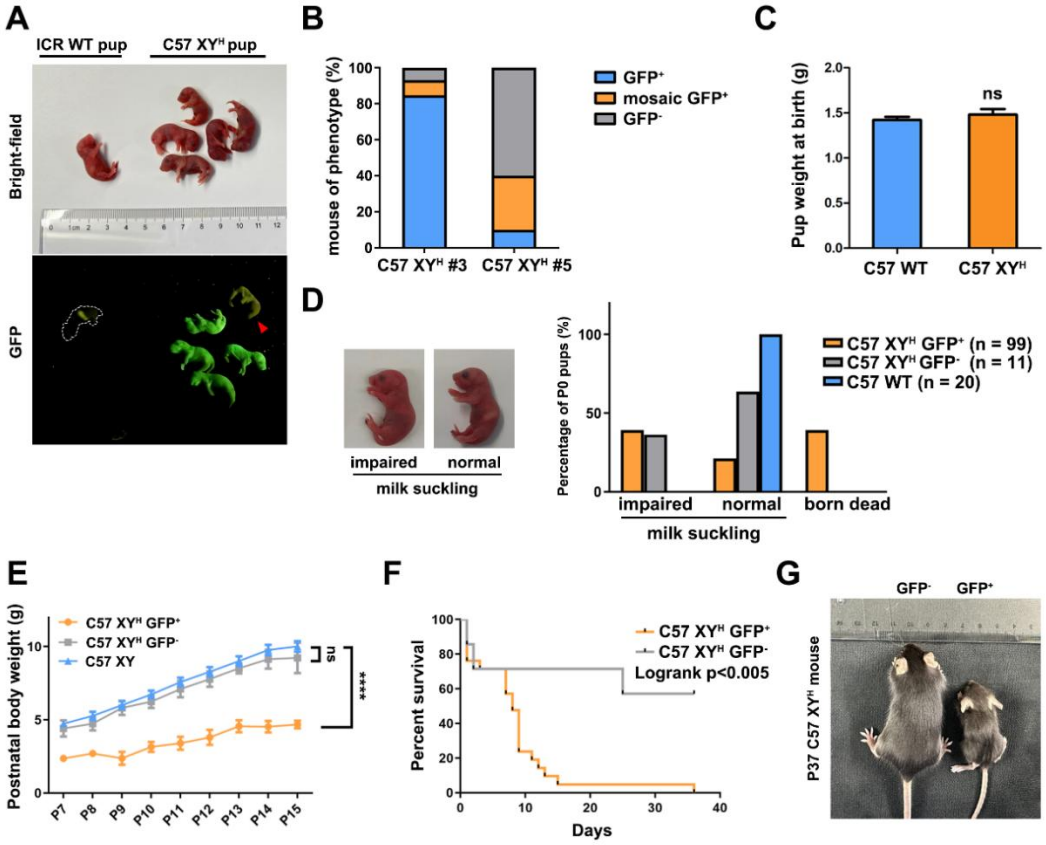

Figure 4 Neonatal mortality and impaired growth in C57 XY^H mice

A. Generation of full-term C57 XY^H pups. Photographs are shown on the top, and images for GFP signals are shown on the bottom. The red arrow indicates a GFP$^-$ C57 XY^H pup.

B. Composition of neonatal tetraploid complementation mice derived from C57 XY^H #3 and C57 XY^H #5 ESCs. Mice were categorized into three phenotypic groups based on GFP expression: GFP$^+$ (fully GFP-positive, blue), mosaic GFP$^+$ (partially GFP-positive, orange), and GFP$^-$ (GFP-negative, gray). The proportions of each phenotype are shown for both ESC lines.

C. Body weights of wild-type C57BL/6 (n = 8) and C57 XY^H (n = 11) newborn pups. ns, not significant.

D. Left, 24 h after birth, neonatal pups with low amount or no milk in the stomach were classified as the impaired milk suckling group, while those with visible milk in the stomach were classified as the normal milk suckling group. Right, percentages of wild-type C57BL/6 (C57 WT; n = 20), C57 XY^H GFP$^+$ (n = 99), and C57 XY^H GFP$^-$ (n = 11) neonatal pups that were categorized into three phenotypic groups.

E. Postnatal body weight progression of three tetraploid complementation mouse groups: male C57BL/6 (C57 XY; n = 5), C57 XY^H GFP$^+$ (n = 5), and C57 XY^H GFP$^-$ (n = 5). Body weight was measured from P7 to P15. Data are presented as mean ± SEM. ****$p < 0.0001$, Repeated Measures ANOVA; ns, not significant.

F. Kaplan-Meier Survival curves of C57 XY^H GFP$^+$ (n = 21) and C57 XY^H GFP$^-$ (n = 7) mice. The survival rate was monitored over 40 days. Statistical significance was determined using the log-rank test ($p < 0.005$).

G. Representative images of P37 C57 XY^H mice. The body size of GFP$^+$ mouse was smaller compared to its GFP$^-$ littermates (n = 4).

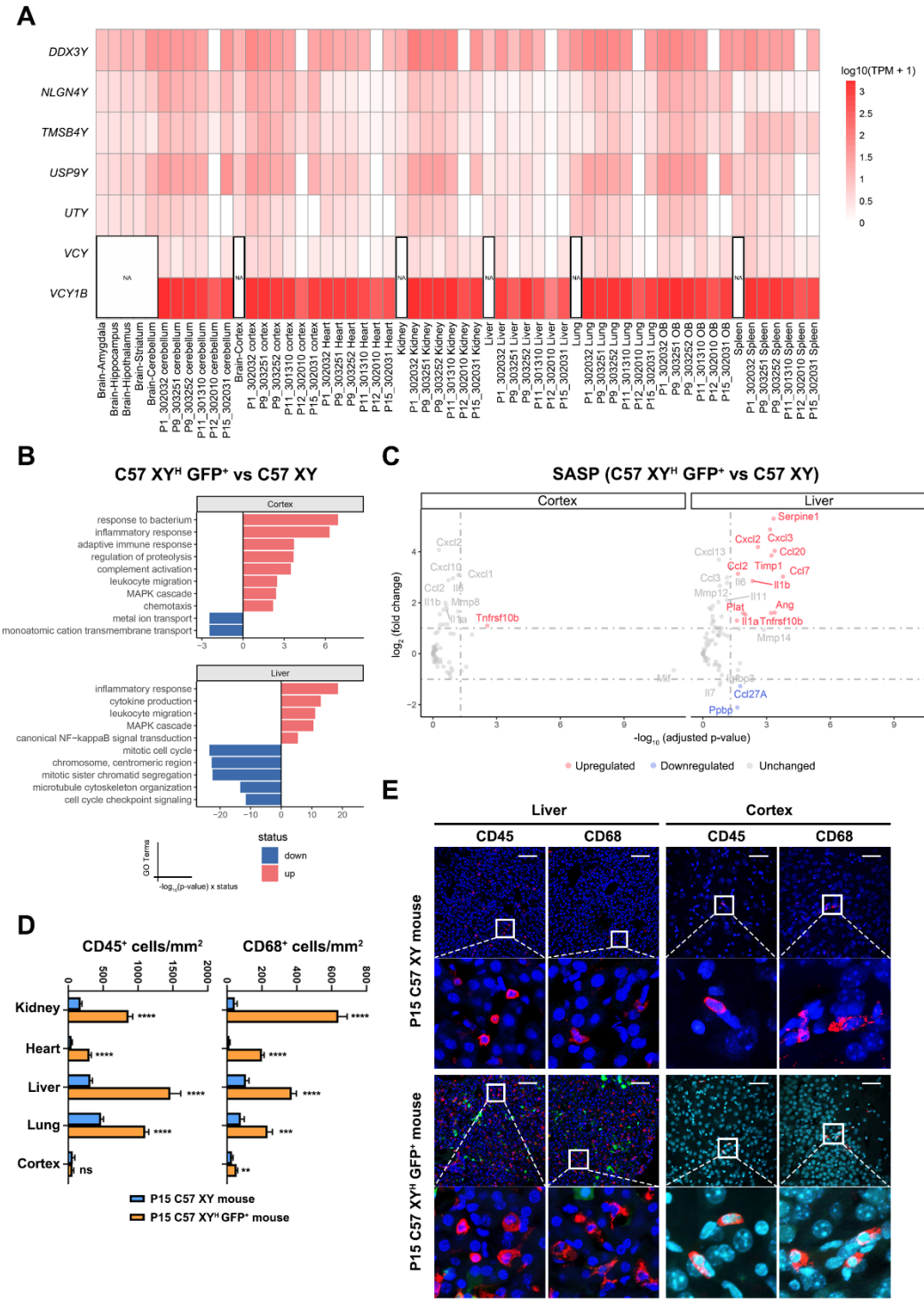

Figure 5 Transcriptomic alteration and inflammation in C57 XY^{H} mice

A. The human chrY genes obtained from various tissues were selected for heatmap assay. The sample labeled by mouse age, identifier and organ (e.g., P9_303252 cerebellum) was extracted from C57 XY^{H} GFP^{+} mice aged P1 to P15 (n = 6). The sample labeled solely by organ (e.g., Brain-Amygdala, Kidney) are derived from previously published data[25].

B. Gene Ontology (GO) enrichment analysis of DEGs in the liver and cortex of C57 XY^{H} GFP^{+} mice versus male C57BL/6 mice (C57 XY).

C. Scatter plots showing the differential expression levels of SASP genes in the liver and cortex of

C57 XY^{H} GFP^{+} mice compared to male C57BL/6 mice (C57 XY).

D. The density of CD45- and CD68-positive cells was quantified as the number of cells per mm^2 (n = 20 each). Data are presented as mean ± SEM. **p < 0.01, ***p < 0.001, ****p < 0.0001, unpaired two-tailed Student's t test. ns, not significant. C57 XY mouse, male C57BL/6 mouse.

E. Liver and cortex of P15 male C57BL/6 (C57 XY) and P15 C57 XY^{H} GFP^{+} mice were immunostained for CD45 or CD68 (red). Hoechst (blue) was used to label DNA. Scale bars, 50 μm.

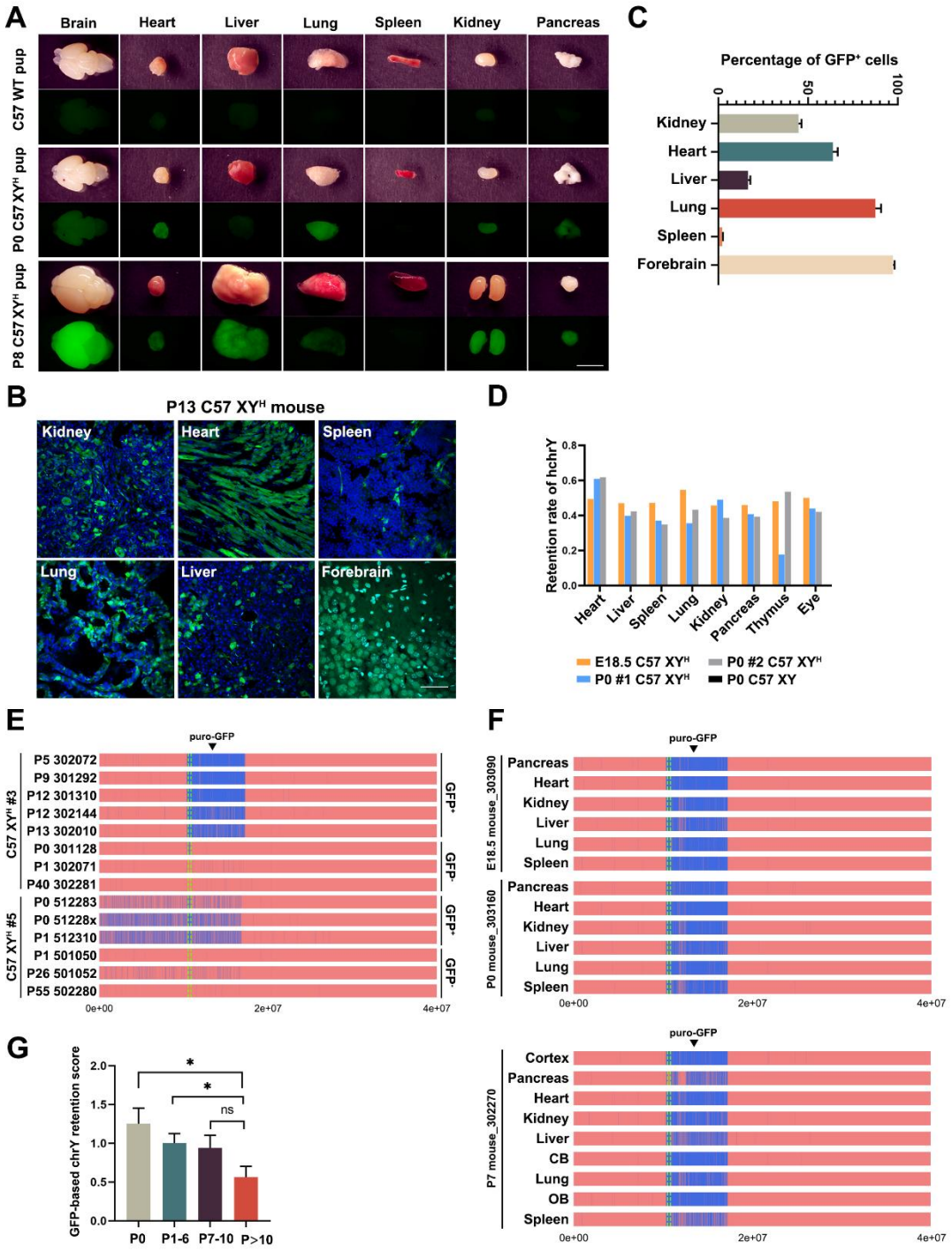

Figure 6 Variable GFP expression and Y chromosomal instability in C57 XY^{H} mice

A. Morphology of different organs in wild-type C57BL/6 (C57 WT), P0 C57 XY^{H} and P8 C57 XY^{H} pups. The images for GFP signals are shown in the bottom row. Scale bar, 5 mm.

B. Representative images showing the percentage of GFP^{+} cells among different tissues in P13 C57 XY^{H} mouse. Scale bar, 400 μm.

C. Percentages of GFP^{+} cells among different tissues in P13-P15 C57 XY^{H} mice (n = 20 per group).

D. Retention of human chrY in different organs of C57 XY^H (E18.5 C57 XY^H, P0 #1 C57 XY^H, P0 #2 C57 XY^H) and male C57BL/6 (P0 C57 XY), which was determined by real-time genomic DNA PCR of gene *UTY* on human chrY.

E. Human chrY content in tail genomic DNA of C57 XY^H #3 and C57 XY^H #5 mice. Mouse identifiers (IDs) are listed on the left. WGS coverage profiles of human chrY across 14 mice are shown, with genomic positions (0.0 - 6×10^7 bp) annotated at bottom. Blue regions represent sequencing read coverage, confirming the presence of Y chromosomal DNA, while red regions denote coverage gaps. The Puro-GFP knock-in site on human chrY is labeled. Corresponding GFP phenotypes for individual mice are displayed on the right.

F. Human chrY content in genomic DNA from various tissues of C57 XY^H #3 mice. Mouse identifiers (IDs) and the age of each mouse (E18.5, P0 and P7) are listed on the left. WGS coverage profiles of human chrY across different tissues are shown, with genomic positions (0.0 - 6×10^7 bp) annotated at bottom. Blue regions represent sequencing read coverage, confirming the presence of Y chromosomal DNA, while red regions denote coverage gaps. The Puro-GFP knock-in site on human chrY is labeled. All these mice are GFP^+.

G. GFP-based chrY retention levels were quantified using WGS data from tail genomic DNA of C57 XY^H mice. For each animal, a GFP-based chrY retention score was calculated as the ratio between the average read depth across the GFP integration region and that of the autosomal reference gene Gapdh (Retention score = GFP depth/Gapdh depth). Mice were grouped according to postnatal survival time (P0, n = 5; P1–6, n = 8; P7–10 n = 4; P>10, n = 5). Data are presented as mean ± SEM. *$p < 0.05$, unpaired two-tailed Student's t test. ns, not significant.

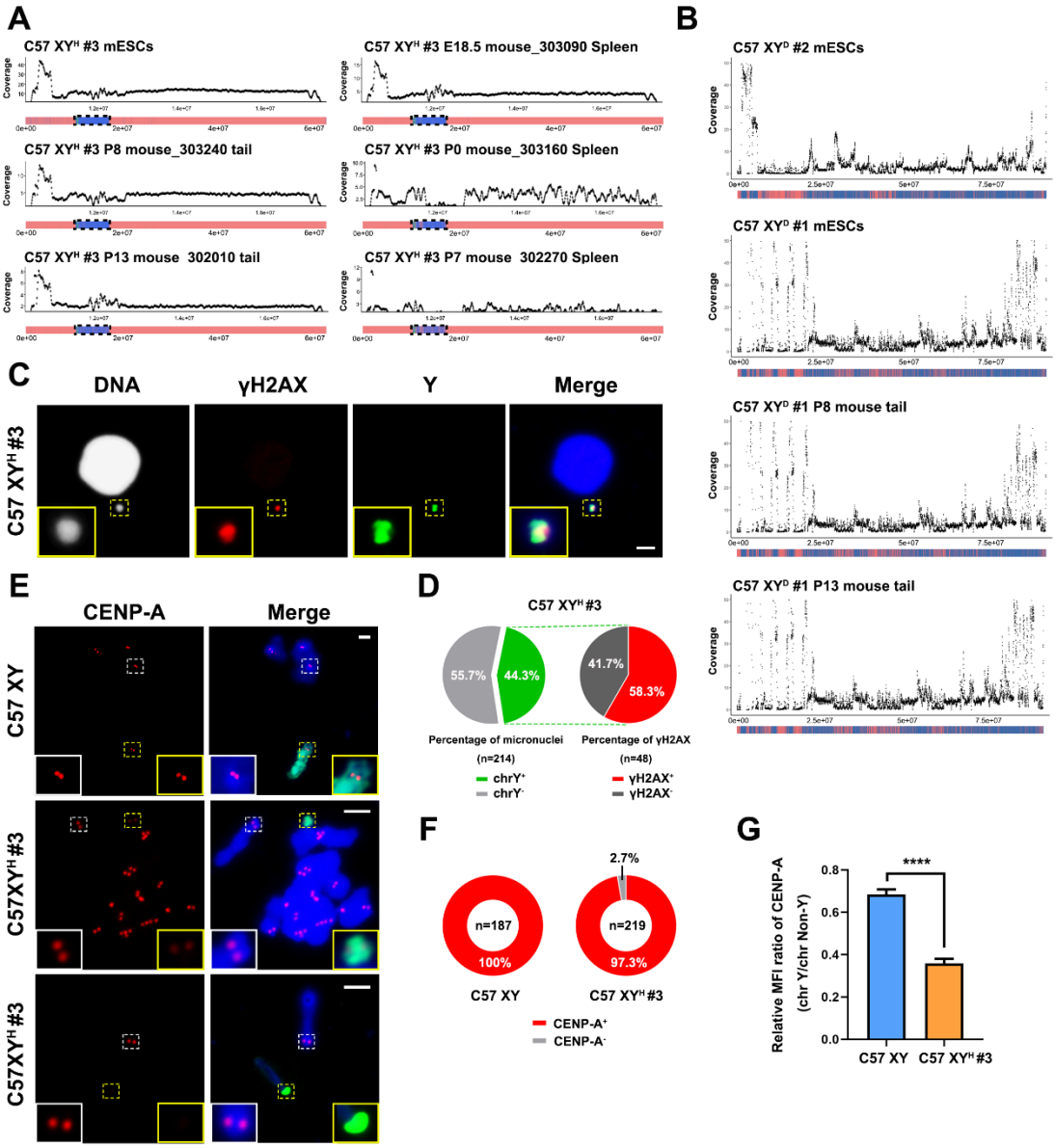

Figure 7 Persistent rearrangements in the transferred human Y chromosome

A. Whole-genome sequencing (WGS) analysis of C57 XYH #3 mESCs and C57 XYH #3 mouse tissues carrying complex human chrY rearrangements exhibiting oscillating DNA copy-number patterns. Human Y-chromosome coverage was calculated using a 50 kb window with a 10 kb step size, while mouse Y-chromosome sequencing depth was computed using 100 bp bins. Each panel represents an individual sample (mESCs, P8 mouse_303240 tail, P13 mouse_302010 tail, E18.5 mouse_303090 spleen, P0 mouse_303160 spleen, and P7 mouse_302270 spleen). Black dots denote sequencing depth across the mappable regions of chrY (horizontal axis). The WGS coverage profile of chrY is shown below the axis: blue regions indicate sequencing read coverage confirming the presence of Y-chromosomal DNA, while red regions denote coverage gaps. The dashed black box highlights the chromosomal region corresponding to the scatter plot above.

B. WGS analysis of C57 XYD mESCs and C57 XYD mouse tails with complex *mouse* chrY rearrangements. Coverage was calculated using a 50 kb window with a 10 kb step size, while

mouse Y-chromosome sequencing depth was computed using 100 bp bins. Each panel represents an individual sample (C57 XYD #1 mESCs, C57 XYD #2 mESCs, P8 C57 XYD #1 mouse tail, and P13 C57 XYD #1 mouse tail).

C. Representative Immuno-FISH images of micronucleated C57 XY^{H} #3 mESCs labelled for DNA (Hoechst, white), γH2AX (red) and human chrY (green). Insets show enlarged images of micronuclei. Scale bar, 5 μm.

D. Proportion of micronuclei containing human chrY and their γH2AX status in C57 XY^{H} #3 mESCs. The left pie chart shows the distribution of human chrY within micronuclei, revealing that 44.3% of the total detected micronuclei (n = 214) contained chrY ($chrY^{+}$), while the remaining 55.7% lack chrY ($chrY^{-}$). The right pie chart represents the percentage of γH2AX-positive ($γH2AX^{+}$, 58.3%) and γH2AX-negative ($γH2AX^{-}$, 41.7%) micronuclei among those carrying human chrY (n = 48).

E. Representative Immuno-FISH images of metaphase spreads prepared from male C57 and C57 XY^{H} #3 mESCs labelled for DNA (Hoechst, blue), CENP-A (red) and chrY (green). Insets provide magnified views of the regions delineated by the dashed boxes, each corresponding to their respective colors. Scale bars, 5 μm.

F. Proportion of $CENP\text{-}A^{+}$ chromosome in male C57BL/6 (C57 XY) and C57 XY^{H} #3 mESCs. Numbers in the middle of the ring indicate the number of sights analyzed per experiment.

G. Mean Fluorescence Intensity of CENP-A on chrY is normalized against the autosome or chrX centromere. Data are presented as mean ± SEM. ****$p < 0.0001$, unpaired two-tailed Student's t test, (C57 XY, n = 30; C57 XY^{H} #3, n = 64).

Supplemental figures

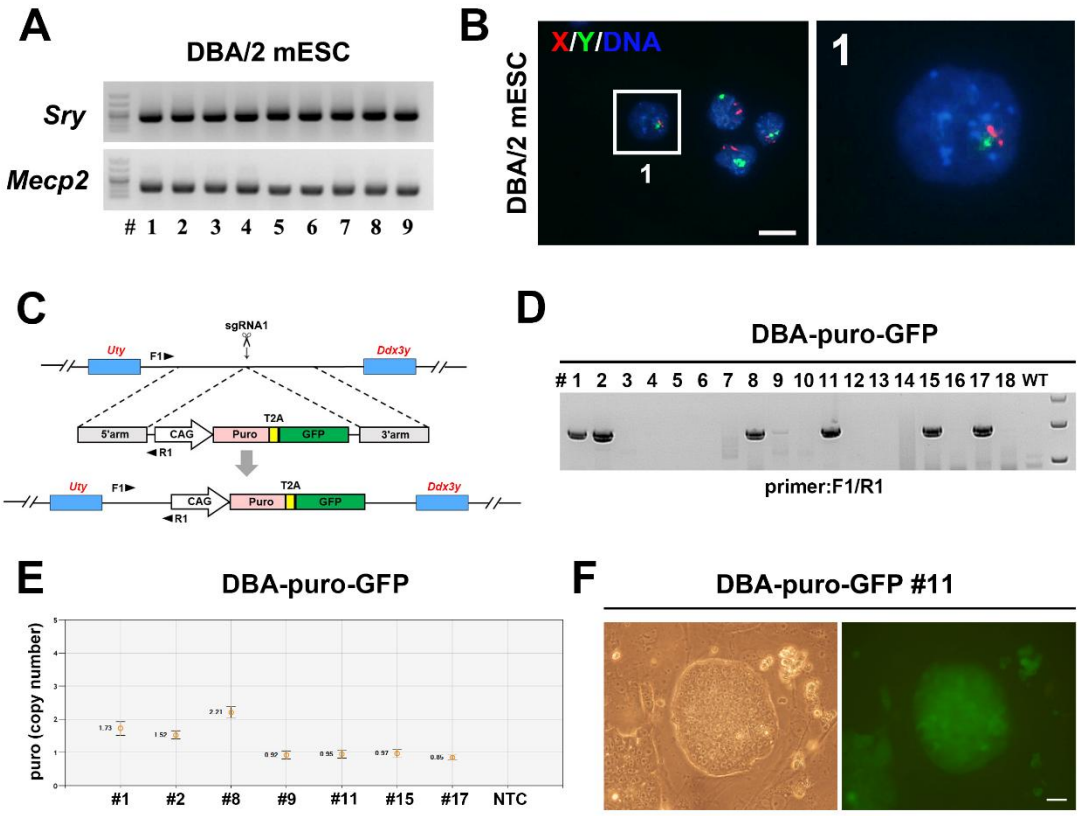

Figure S1 Generation of intraspecies Y chromosome donor cell line

A. Genomic DNA PCR results of nine DBA/2 ESC clones. *Sry* and *Mecp2* are located on chromosome Y and X, respectively.

B. Representative DNA-FISH analysis of DBA/2 ESC clone. Green, whole-chromosome probe for mouse Y chromosome; red, whole-chromosome probe for mouse X chromosome; blue, Hoechst-labeled DNA. Scale bar, 10 μm.

C. Schematic representation of the genome editing strategy for CAG-puro-GFP knock-in in mouse chrY. The positions of the designed primers for genomic PCR are shown as triangles.

D. Genomic DNA PCR results of 18 colonies retrieved from CAG-puro-GFP knock-in. The primers used are indicated in (C).

E. Copy number of puromycin in seven DBA-puro-GFP ESC clones indicated in (D). NTC, No Template Control.

F. Morphology of DBA-puro-GFP ESC line #11. DBA-puro-GFP #11 expressed GFP. Scale bar, 100 μm.

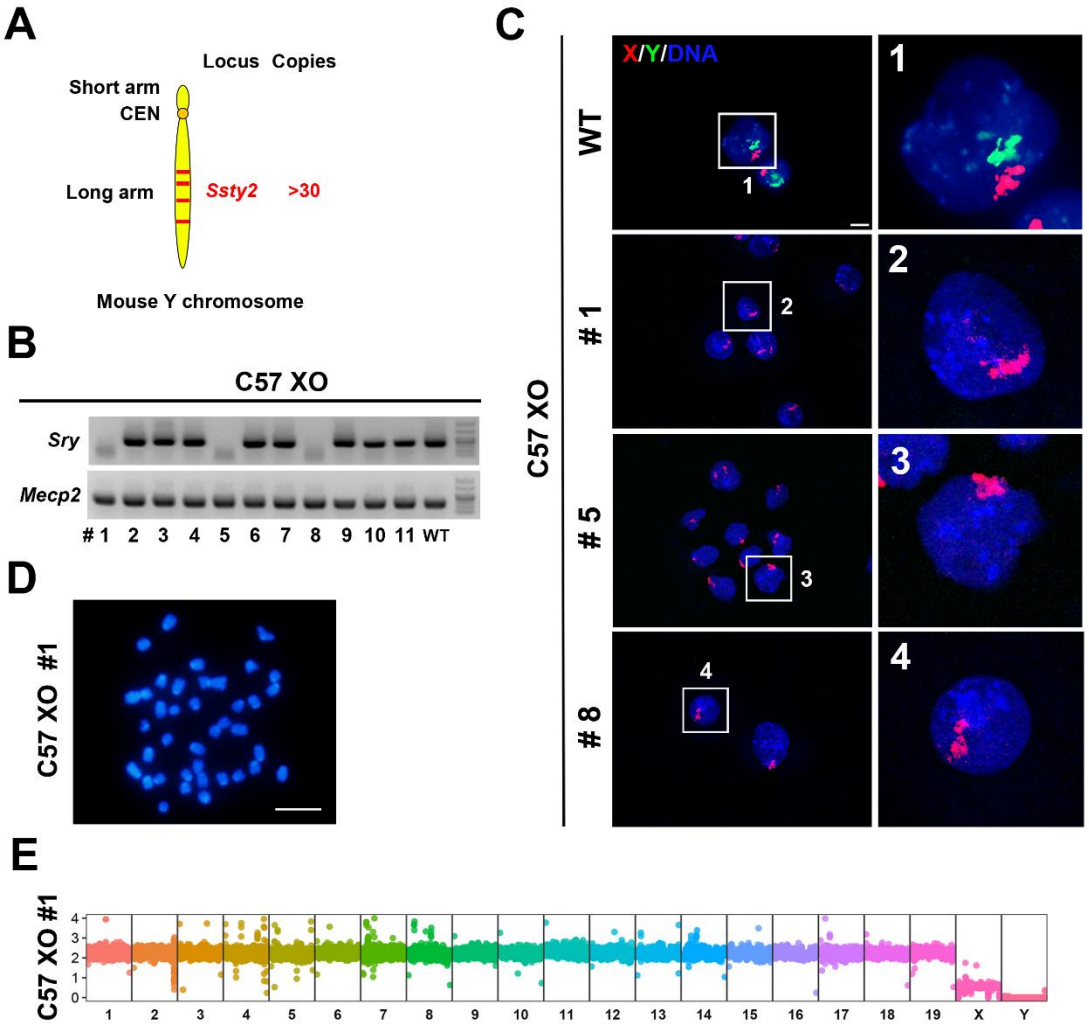

Figure S2 Generation of Y chromosome recipient cell line

A. Targeted gene loci in mouse Y chromosome: *Ssty2*, scattered in the long arm. CEN, centromere.
B. Genomic DNA PCR results of 11 colonies retrieved from C57BL/6 chrY elimination. *Sry* and *Mecp2* are located on chromosome Y and X, respectively.
C. Representative DNA-FISH analysis of male C57 ESC clone and C57 XO ESC clones indicated in (B). Green, whole-chromosome probe for mouse Y chromosome; red, whole-chromosome probe for mouse X chromosome; blue, Hoechst-labeled DNA. Scale bar, 10 μm.
D. Karyotyping of C57 XO ESC line #1 showed 39 instead of 40 chromosomes. Scale bar, 10 μm.
E. WGS showed chrY elimination of C57 XO ESC line #1. The C57 XO #1 showed one copy of the chrX with the chrY absent. Vertical axis, copy number; horizontal axis, chromosome number.

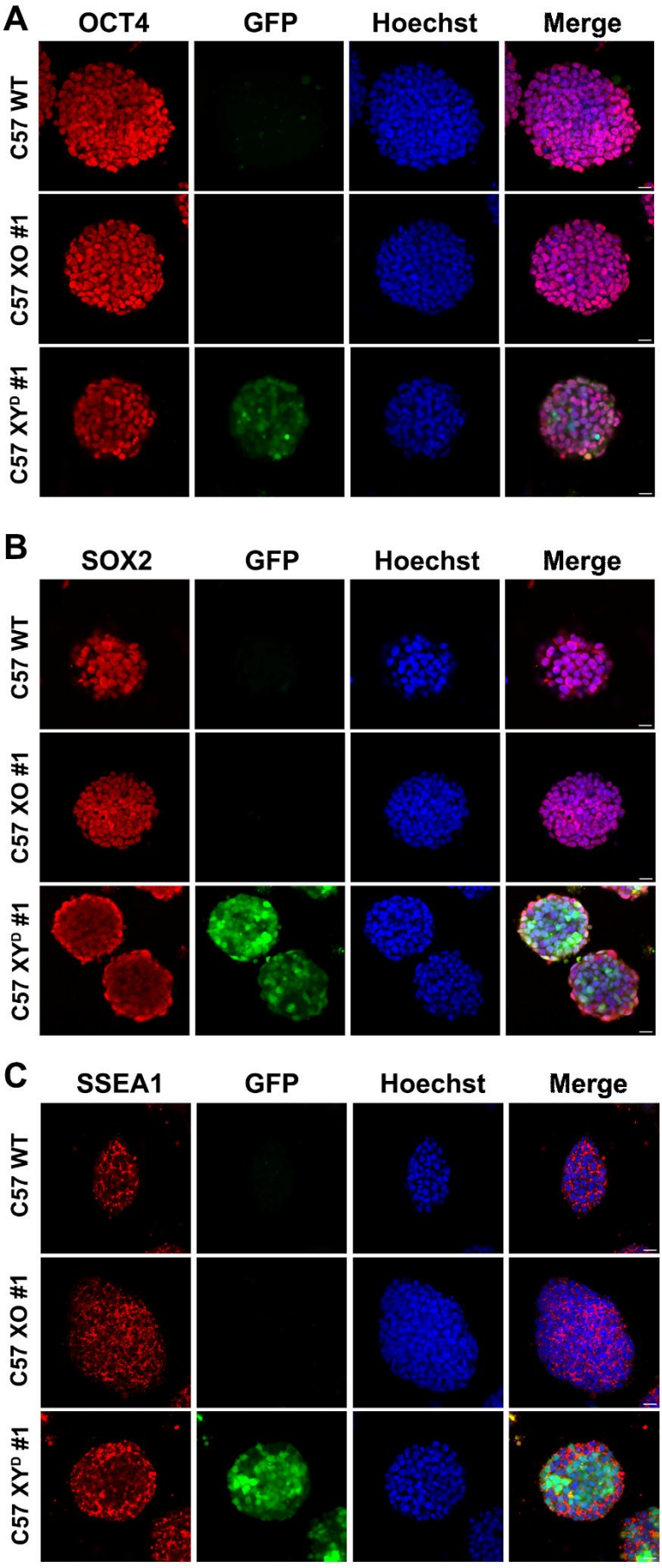

Figure S3 Immunofluorescence staining analysis of pluripotency markers in C57 XY^{D} mESCs

A-C. Immunostaining of pluripotency marker gene Oct4, Sox2 and SSEA1 in wild-type C57BL/6 (C57 WT), C57 XO #1 and C57 XY^{D} #1 ESCs. Scale bars, 20 μm.

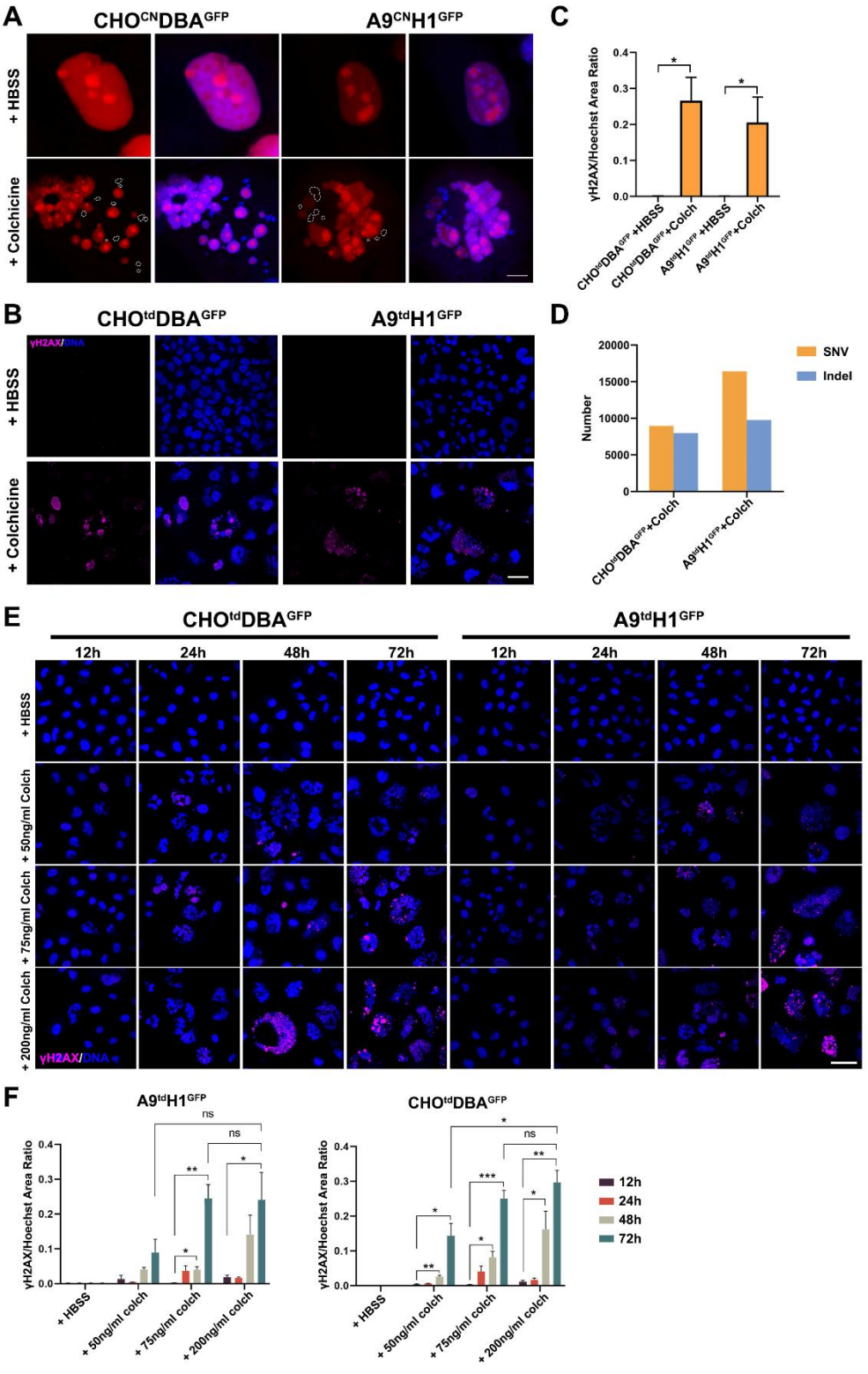

Figure S4 Nuclear envelope instability and DNA damage during MMCT

A – D. Cells treated with 75 ng/ml colchicine for 72 h.

A. Parts of micronuclei in HBSS-treated (+ HBSS) and colchicine-treated (+ Colchicine) CHO^{CN}DBA^{GFP} and A9^{CN}H1^{GFP} cells lose mCherry–NLS, which were marked with dashed lines. Scale bar, 20 μm.

B. Representative immunofluorescence images of HBSS-treated (+ HBSS) and colchicine-treated (+ Colchicine) CHO^{td}DBA^{GFP} and A9^{td}H1^{GFP} cells, stained with Hoechst (blue) and DNA damage marker γH2AX (pink). Scale bar, 50 μm.

C. The ratio of γH2AX-positive area to Hoechst-stained nuclear area indicated in (B) (n = 5 slices per group). Data are presented as mean ± SEM. *p < 0.05, unpaired two-tailed Student's t test.

D. Comparison of number of detected SNVs and indels. The number of SNVs for colchicine-treated CHO^{td}DBA^{GFP} and colchicine-treated A9^{td}H1^{GFP} were 8956 and 16422, respectively. The number of indels for colchicine-treated CHO^{td}DBA^{GFP} and colchicine-treated A9^{td}H1^{GFP} were 7982 and 9766, respectively.

E. Representative immunofluorescence images of CHO^{td}DBA^{GFP} and A9^{td}H1^{GFP} cells following colchicine treatment at varying concentrations (0, 50, 75, and 200 ng/ml) and exposure times (12, 24, 48, and 72 h), stained with Hoechst (blue) and DNA damage marker γH2AX (pink). The 0 ng/ml group is labeled as "+ HBSS". Scale bar, 50 μm.

F. The ratio of γH2AX-positive area to Hoechst-stained nuclear area indicated in (E) (n = 3 slices per group). Data are presented as mean ± SEM. *p < 0.05, **p < 0.01, ***p < 0.001, unpaired two-tailed Student's t test. ns, not significant.

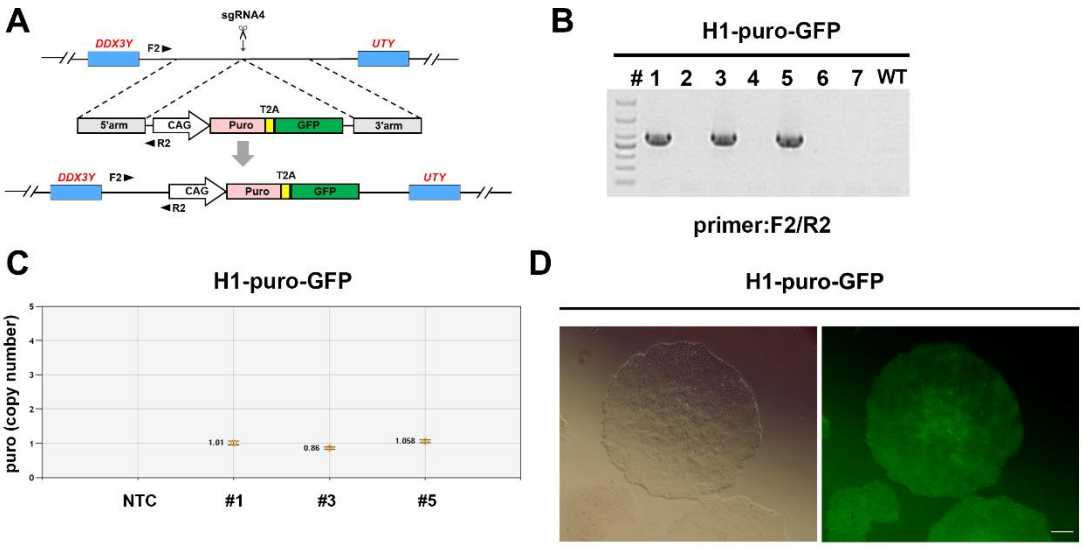

Figure S5 Generation of interspecies Y chromosome donor cell line

A. Schematic representation of the genome editing strategy for CAG-puro-GFP knock-in in human chrY. The positions of the designed primers for genomic PCR are shown as triangles.

B. Genomic DNA PCR results of 7 colonies retrieved from CAG-puro-GFP knock-in. The primers used are indicated in (A). WT, H1 human ESC.

C. ddPCR results of three H1-puro-GFP ESC clones. Copy number of puromycin in three H1-

puro-GFP ESC clones indicated in (B). NTC, No Template Control.

D. Morphology of H1-puro-GFP ESC line. H1-puro-GFP ESCs expressed GFP. Scale bar, 250 μm.

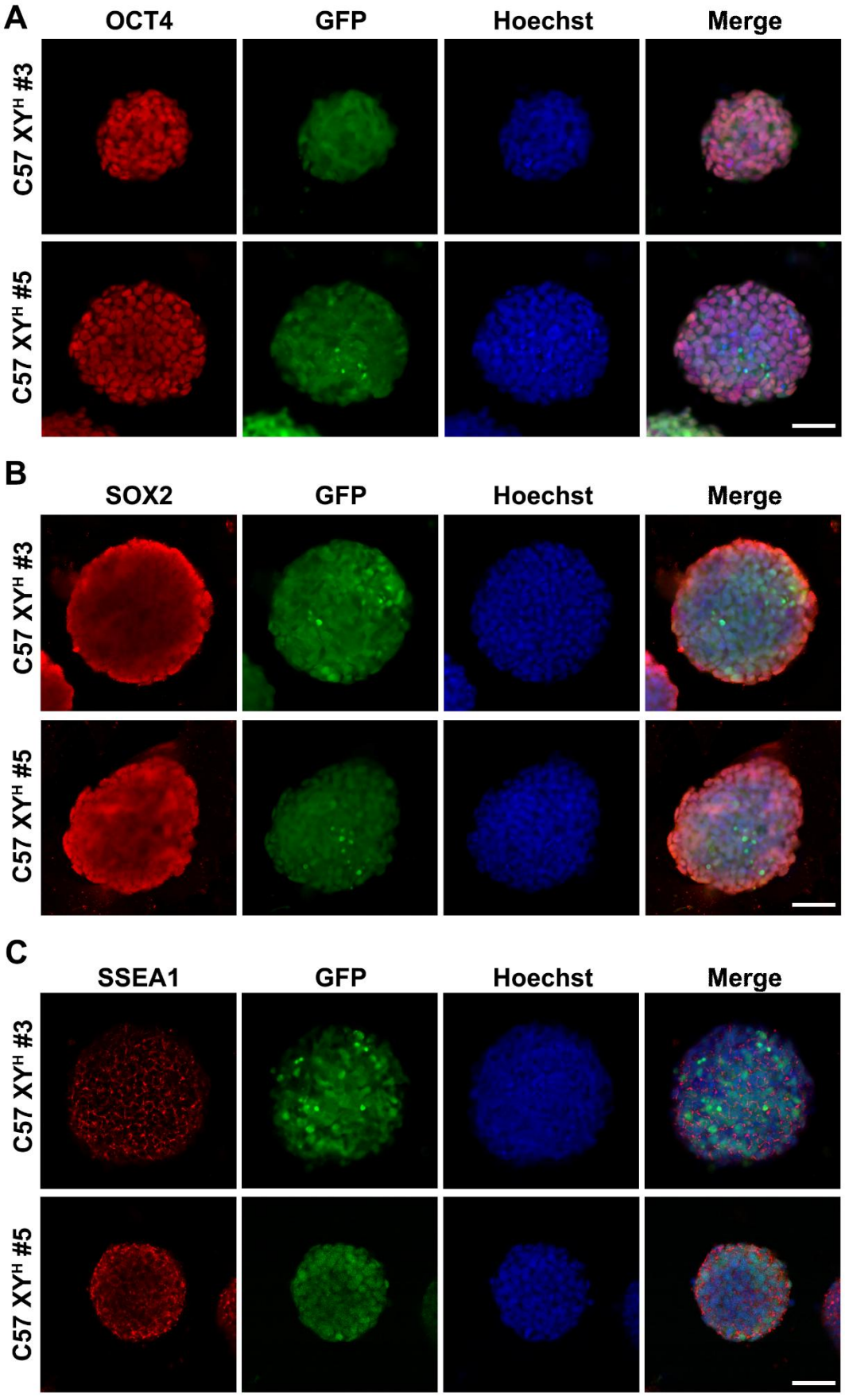

Figure S6 Immunofluorescence staining analysis of pluripotency markers in C57 XY^{H} mESCs

A-C. Immunostaining of pluripotency marker gene Oct4, Sox2 and SSEA1 in C57 XY^{H} #3 and C57 XY^{H} #5 ESCs. Scale bars, 50 μm.

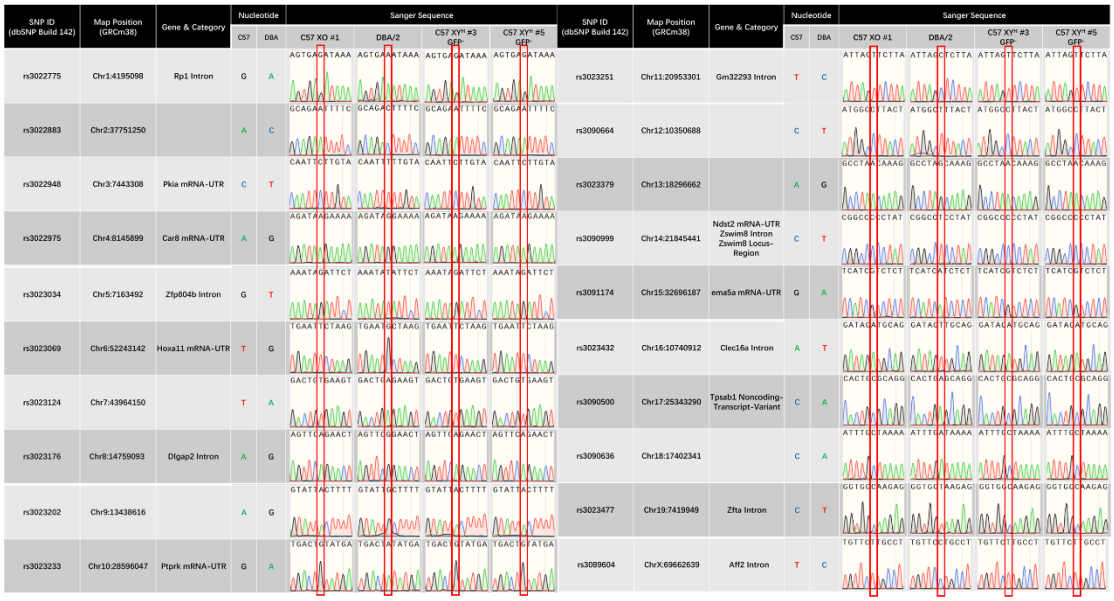

Figure S7 Genotyping of SNP loci with sequence variations between C57BL/6 and DBA/2 mice.

A. The table lists SNP loci with sequence variations between C57BL/6 and DBA/2 mice. Nucleotide differences are highlighted in red boxes. Representative genotyping results are shown for individual mice from four strains: C57 XO #1, DBA/2, C57 XY^{H} #3 GFP^{-}, and C57 XY^{H} #5 GFP^{-}. Notably, C57 XY^{H} #3 GFP^{-} and C57 XY^{H} #5 GFP^{-} mice exclusively retain C57-specific alleles at all SNP loci. SNP positions are annotated with chromosome position (GRCm38 assembly) and gene categories (e.g., intronic, mRNA-UTR).

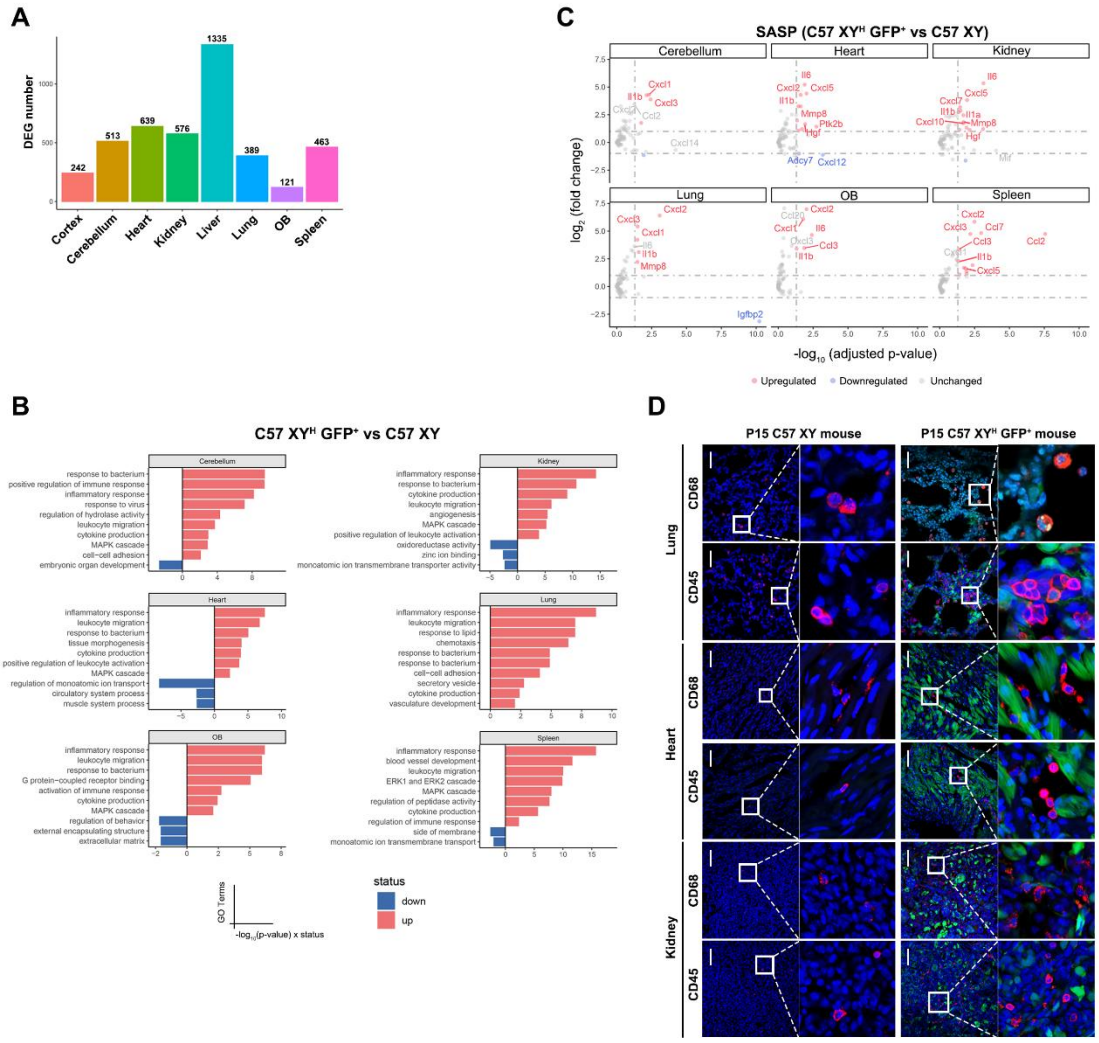

Figure S8 Activation of inflammatory responses in C57 XY^{H} GFP^{+} mice

A. The number of differentially expressed genes across various organs in C57 XY^{H} GFP^{+} mice compared to male C57BL/6 mice from postnatal day 1 to day 15 (n = 11). OB, Olfactory bulbs.

B. Gene Ontology (GO) enrichment analysis of DEGs across various tissues in C57 XY^{H} GFP^{+} mice compared to male C57BL/6 mice. OB, Olfactory bulbs.

C. Scatter plots showing the differential expression levels of SASP genes across various tissues in C57 XY^{H} GFP^{+} mice compared to male C57BL/6 mice. OB, Olfactory bulbs.

D. Various tissues of P15 male C57BL/6 and P15 C57 XY^{H} GFP^{+} mice were immunostained for CD45 or CD68 (red). Hoechst (blue) was used to label DNA. Scale bars, 50 μm.